



# Multiscale analysis of elastic waves in soft materials: From molecular chain networks to fiber composites

Nitesh Arora<sup>1,\*</sup>, Yuhai Xiang<sup>1</sup>, Stephan Rudykh

Department of Mechanical Engineering, University of Wisconsin – Madison, Madison, WI 53706, United States

## ARTICLE INFO

### Keywords:

Soft materials  
Wave propagation  
Microstructure  
Polymer chains  
Fiber composites  
Multiscale analysis

## ABSTRACT

We provide a multiscale analysis of elastic waves in soft microstructured materials including the underlying molecular chain network mechanisms and micromechanics of hyperelastic fiber composites. First, we examine the interplay between the crosslinked and entangled polymer chains and elastic wave characteristics in finitely deformed materials. Next, we study the shear wave propagation in a class of heterogeneous hyperelastic composites. In particular, we consider the transversely isotropic fiber composites with phases characterized by the stiffening behavior stemming from the non-Gaussian statistics of polymer chains. By employing a micromechanics-based approach, we derive explicit expressions for phase velocities in terms of material properties and volume fraction of the phases. Our results indicate the significant influence of the variety of length-scales mechanisms on the elastic wave characteristics. We provide examples to illustrate the influence of the mechanisms under different loading conditions, wave propagation directionality, and material microstructure parameters.

## 1. Introduction

Understanding of elastic wave propagation is essential for a variety of applications including non-invasive evaluation [1–3], waveguides [4–6], and medical imaging [7]. Moreover, acoustic or mechanical metamaterials offer ways to achieve desirable or unusual wave characteristics [8], such as frequency filtering [9], cloaking [10], negative phase and group velocities [11,12]. In turn, soft microstructured materials open the possibility of controlling and tuning these properties through deformation [13–17]. Remarkably, even the acoustic characteristics of comparatively simple homogeneous soft materials can be significantly transformed by deformation [18,19]. For instance, soft hyperelastic materials can be used to split pressure and shear waves [20,21]. Furthermore, soft materials can develop large deformations in response to external stimuli [22–28], therefore, the wave characteristics can also be controlled remotely, for example, by magnetic field [29–32].

Soft materials exhibit very rich and complex mechanical behavior by virtue of their underlying microstructures at different length-scales. At *microscale*, for instance, biphasic microstructures are widely present in natural and biological soft materials, simultaneously providing them with high strength, lightweight, and flexibility. For example, fiber-matrix microstructure (schematically shown in Fig. 1(a)) is notably found in many soft biological tissues [33], such as tendons and ligaments [34]. At *molecular* length-scales, the microstructure is de-

fined by the long molecular chain networks. These networks consist of crosslinked and entangled polymer chains [35–39] (schematically shown in Fig. 1(b)). While the connection of these microstructures with the static macroscopic mechanical behavior of soft materials have been investigated actively [40–43], less is known about the influence of microscopic parameters on the elastic wave characteristics. In this paper, we provide a multiscale analysis of elastic wave propagation in soft microstructured materials.

In regard to the analysis of elastic wave propagation, the framework of small amplitude motions superimposed on finite deformations is widely used. The seminal work of Biot [44] laid the foundation for the wave propagation analysis in finitely deformed homogeneous isotropic materials. By the application of the invariant theory, Destrade and Ogden [45] generalized the problem of infinitesimal wave propagation in finitely deformed hyperelastic materials. Scott and Hayes [46] employed the nonlinear elastic theory [47] together with the phenomenological constitutive approach to study small-amplitude plane waves superimposed on homogeneous deformation in the fiber-reinforced materials with inextensible fibers. Scott [48,49] generalized the analysis for a broader class of anisotropic materials. Ogden and Singh [50] revisited the problem for transversely isotropic (TI) solids with the presence of initial stresses. In particular, Ogden and Singh [50] used the phenomenological theory of invariants and presented a clear formulation for small-amplitude wave propagation in incompressible TI hyperelastic materials. This methodology was used for analyzing homogeneous

\* Corresponding author.

E-mail address: [narora7@wisc.edu](mailto:narora7@wisc.edu) (N. Arora).

<sup>1</sup> Equal contribution

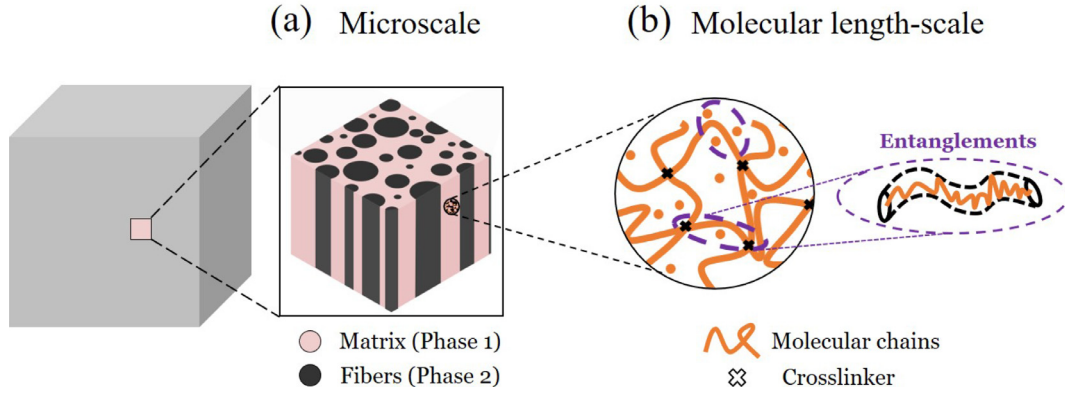


**Fig. 1.** Schematic of microstructures present in soft matter at different length-scales. (a) Microscale – biphasic fiber-matrix microstructure, and (b) Molecular length-scale – crosslinked and entangled polymer chains.

plane waves (see Vinh and Merodio [51]) and non-principal Rayleigh waves (see Nam et al. [52], Vinh et al. [53]) in various TI solids.

Recently, Galich et al. [54] employed a micromechanics-based approach to study the wave propagation in finitely deformed 3D fiber composites (FCs). They also investigated the influence of the composite microstructure parameters on the elastic wave characteristics. More recently, Galich et al. [55] employed the Bloch wave analysis to study the periodic 3D fiber composites having neo-Hookean constituents with various in-plane periodicity. While the studies by Galich et al. [54,55] account for the spatial distribution of phases, they consider composites with weakly non-linear neo-Hookean hyperelastic phases. Soft materials, however, exhibit strong nonlinearities, especially prominent at large strain levels. For example, the stiffening behavior, which can be captured using the non-Gaussian polymer network statistics [56]. As we shall show, such nonlinear effects significantly influence the elastic wave characteristics of homogeneous as well as heterogeneous soft materials.

In the first part of our paper, Sec. 3, we study the elastic wave characteristics of isotropic soft elastomers with a special focus on the influence of inter-molecular polymer chain entanglements. We employ a constitutive model accounting for the crosslinking and entanglement of polymer chains [57]. Based on the entangled network (EN) model, we derive explicit expressions of phase velocities for various deformation modes and wave directionality, and illustrate the role of entanglement of polymer chains on the elastic wave characteristics. Next, in Sec. 4, we examine the shear wave propagation in the transversely isotropic 3D FCs with stiffening phases. We employ a micromechanics-based approach and derive the explicit expression for the wave velocities. We obtain the important wave characteristic in terms of volume fraction and material properties of the phases, for general propagation direction. Using the derived relations, we categorically show the influence of the stiffening behavior of phases and applied deformation on the shear wave propagation in FCs. To begin with, in Sec. 2, we provide the theoretical background on finite elasticity and small amplitude motions superimposed on finite deformations.

## 2. Theoretical background

Consider a continuum body, in which each point is identified by its position vector  $\mathbf{X}$  in the undeformed configuration. In the deformed configuration, the new position vector  $\mathbf{x}(\mathbf{X})$  defines the location of the corresponding points. The deformation gradient is defined as  $\mathbf{F} = \partial \mathbf{x} / \partial \mathbf{X}$ , and its determinant is  $J \equiv \det \mathbf{F} > 0$ . Consider a hyperelastic material with a strain energy density function (SEDF),  $\psi(\mathbf{F})$ , thus, the first Piola-Kirchhoff stress tensor is

$$\mathbf{P} = \frac{\partial \psi(\mathbf{F})}{\partial \mathbf{F}}. \quad (1)$$

For an incompressible material,  $J = 1$ , and Eq. (1) modifies as

$$\mathbf{P} = \frac{\partial \psi(\mathbf{F})}{\partial \mathbf{F}} - p \mathbf{F}^{-T}, \quad (2)$$

where  $p$  is an unknown Lagrange multiplier.

In the undeformed configuration, the equation of motion for quasi-static deformation and without any body forces is written as

$$\nabla \cdot \mathbf{P} = \mathbf{0}. \quad (3)$$

Next, consider small-amplitude motions superimposed on the finitely deformed state. The incremental equation of motion is

$$\nabla \cdot \dot{\mathbf{P}} = \rho_0 \frac{D^2 \mathbf{u}}{Dt^2}, \quad (4)$$

where  $\rho_0$  is the initial mass density,  $\dot{\mathbf{P}}$  is the incremental change in the 1<sup>st</sup> Piola-Kirchhoff stress tensor, and  $\mathbf{u}$  is the incremental displacement, related to the corresponding change in the deformation gradient as  $\dot{\mathbf{F}} = \nabla \mathbf{u}$ . The linearized constitutive law is

$$\dot{\mathbf{P}} = \mathbb{A}^0 : \dot{\mathbf{F}}, \quad (5)$$

where  $\mathbb{A}^0$  is the tensor of elastic moduli defined as

$$\mathbb{A}^0 = \frac{\partial^2 \psi(\mathbf{F})}{\partial \mathbf{F} \partial \mathbf{F}}. \quad (6)$$

Substitution of Eq. (5) into Eq. (4) yields

$$A_{ijkl}^0 u_{k,lj} = \rho_0 \frac{D^2 u_i}{Dt^2}. \quad (7)$$

In the updated Lagrangian form, Eq. (7) can be written as

$$A_{ijkl} u_{k,lj} = \rho \frac{\partial^2 u_i}{\partial t^2}, \quad (8)$$

where  $A_{ipkq} = J^{-1} A_{ijkl}^0 F_{pj} F_{ql}$  is the updated tensor of elastic moduli, and  $\rho = J^{-1} \rho_0$  is the current mass density.

We seek a solution for Eq. (8) in the form of plane waves with constant polarization

$$\mathbf{u} = \mathbf{m} f(\mathbf{n} \cdot \mathbf{x} - ct), \quad (9)$$

where  $\mathbf{m}$  is a unit vector denoting the polarization;  $\mathbf{n}$  is a unit vector along the wave propagation direction;  $f$  is a twice continuously differentiable function, and  $c$  is the wave phase velocity. Substituting the solution (9) into (8), we obtain

$$\mathbf{Q}(\mathbf{n}) \cdot \mathbf{m} = \rho c^2 \mathbf{m}, \quad (10)$$

where  $\mathbf{Q}$  is the acoustic tensor defined as

$$Q_{ik} = A_{ijkl} n_j n_l. \quad (11)$$

For incompressible materials, Eq. (8) modifies as

$$A_{ijkl} u_{k,lj} + \dot{p}_{,i} = \rho \frac{\partial^2 u_i}{\partial t^2}. \quad (12)$$

The incompressibility implies that  $\nabla \cdot \mathbf{u} = 0$ , and combined with Eq. (9) it yields

$$\mathbf{m} \cdot \mathbf{n} = 0. \quad (13)$$

Substituting the displacement solution form (9) together with  $\dot{\rho} = \rho_0 f(\mathbf{n} \cdot \mathbf{x} - ct)$  into (12) and using (13), we obtain

$$\hat{\mathbf{Q}}(\mathbf{n}) \cdot \mathbf{m} = \rho c^2 \mathbf{m}, \quad (14)$$

where  $\hat{\mathbf{Q}} = \hat{\mathbf{I}} \cdot \mathbf{Q} \cdot \hat{\mathbf{I}}$  and  $\hat{\mathbf{I}} = \mathbf{I} - \mathbf{n} \otimes \mathbf{n}$ .

### 3. Shear waves characteristics of elastomers with crosslinked and entangled molecular chain network

In this section, we study the relations between polymer molecular chain mechanisms and elastic wave propagation. In particular, we examine the role of the *crosslinked networks* and *entangled chains* on shear wave propagation in incompressible soft elastomers. To this end, we consider a SEDF consisting of two parts responsible for crosslinked networks and entanglements [57], namely,

$$\psi = G_c N \ln \left( \frac{3N + I_1/2}{3N - I_1} \right) + G_e \sum_{i=1}^3 \frac{1}{\lambda_i}, \quad (15)$$

where  $I_1$  is the first invariant of the right Cauchy-Green deformation tensor  $\mathbf{C} = \mathbf{F}^T \mathbf{F}$ ; and  $\lambda_i$  ( $i = 1, 2, 3$ ) are the principal stretches; recall that the principal stretches of the right and left Cauchy-Green deformation tensors coincide,  $\lambda_i(\mathbf{C}) = \lambda_i(\mathbf{B})$ , where  $\mathbf{B} = \mathbf{F} \mathbf{F}^T$ . For incompressible materials,  $\lambda_1 \lambda_2 \lambda_3 = 1$ , and  $I_1 = \lambda_1^2 + \lambda_2^2 + \lambda_3^2$ . The initial elastic moduli of the crosslinked network ( $G_c$ ) and entanglements ( $G_e$ ) are related to the microscopic molecular chain quantities via

$$G_c = n k_B T \quad \text{and} \quad G_e = \alpha n N k_B T \frac{b^2}{3d_0^2}, \quad (16)$$

where  $n$  is the number of chains per unit volume (or chain number density) of the crosslinked chains;  $N$  is the number of the Kuhn monomers per chain and  $b$  is the length of the Kuhn monomer;  $k_B$  is the Boltzmann constant and  $T$  is Kelvin temperature;  $\alpha$  is the geometrical parameter and  $d_0$  represents the equivalent diameter of the tube characterizing the entanglement constraints (see Xiang et al. [57] for additional details).

The acoustic tensor corresponding to the SEDF (15) is

$$\hat{\mathbf{Q}}(\lambda_1, \lambda_2, \mathbf{n}) = q_1 \hat{\mathbf{I}} - q_2 \hat{\mathbf{I}} \cdot \mathbf{B} \cdot \hat{\mathbf{I}} + q_3 \hat{\mathbf{I}} \cdot (\mathbf{B} \cdot \mathbf{n} \otimes \mathbf{B} \cdot \mathbf{n}) \cdot \hat{\mathbf{I}} - q_4 [\hat{\mathbf{I}} \cdot (\mathbf{B} \cdot \mathbf{B} \cdot \mathbf{n} \otimes \mathbf{B} \cdot \mathbf{n}) \cdot \hat{\mathbf{I}} + \hat{\mathbf{I}} \cdot (\mathbf{B} \cdot \mathbf{n} \otimes \mathbf{B} \cdot \mathbf{B} \cdot \mathbf{n}) \cdot \hat{\mathbf{I}}] + q_5 \hat{\mathbf{I}} \cdot (\mathbf{B} \cdot \mathbf{B} \cdot \mathbf{n} \otimes \mathbf{B} \cdot \mathbf{B} \cdot \mathbf{n}) \cdot \hat{\mathbf{I}}. \quad (17)$$

Here, the expressions for the scalar coefficients  $q_i$  are given in Appendix A, and  $\mathbf{B} = \mathbf{F} \mathbf{F}^T$  is the left Cauchy-Green deformation tensor. Let us adopt the coordinate system defined by the orthogonal unit vectors  $\mathbf{e}_1, \mathbf{e}_2, \mathbf{e}_3$  coinciding with the principal directions of  $\mathbf{B}$ . Subsequently, for an incompressible material, the deformation gradient is  $\mathbf{F} = \lambda_1 \mathbf{e}_1 \otimes \mathbf{e}_1 + \lambda_2 \mathbf{e}_2 \otimes \mathbf{e}_2 + (\lambda_1 \lambda_2)^{-1} \mathbf{e}_3 \otimes \mathbf{e}_3$ . The corresponding phase velocities of two distinct shear waves are

$$c^{(1)} = \sqrt{a_1/\rho_0} \quad \text{and} \quad c^{(2)} = \sqrt{a_2/\rho_0}, \quad (18)$$

where  $a_1$  and  $a_2$  are the eigenvalues of the acoustic tensor given by Eq. (17) (with their eigenvectors perpendicular to  $\mathbf{n}$ ). In general, the two phase velocities in Eq. (18) are distinct, however, for some special cases they can be identical. For example, shear waves traveling in the principal direction of the left Cauchy-Green deformation tensor ( $\mathbf{n} = \mathbf{e}_i$ ) with  $\lambda_i = \lambda_j^{-2} = \lambda_k^{-2}$  ( $i, j, k = 1, 2, 3$ , and  $i \neq j \neq k$ ) have identical phase velocities

$$c^{(1)} = c^{(2)} = \sqrt{(q_1 - q_2 \lambda_i^{-1})/\rho_0}. \quad (19)$$

In the following, we specify the results for the uniaxial, equi-biaxial, and pure shear finite deformation modes. The corresponding deformation gradients are

$$\begin{aligned} \mathbf{F}^{(u)} &= \lambda \mathbf{e}_1 \otimes \mathbf{e}_1 + \lambda^{-1/2} (\mathbf{I} - \mathbf{e}_1 \otimes \mathbf{e}_1), \\ \mathbf{F}^{(eb)} &= \lambda (\mathbf{e}_1 \otimes \mathbf{e}_1 + \mathbf{e}_2 \otimes \mathbf{e}_2) + \lambda^{-2} \mathbf{e}_3 \otimes \mathbf{e}_3, \quad \text{and} \\ \mathbf{F}^{(ps)} &= \lambda \mathbf{e}_1 \otimes \mathbf{e}_1 + \mathbf{e}_2 \otimes \mathbf{e}_2 + \lambda^{-1} \mathbf{e}_3 \otimes \mathbf{e}_3, \end{aligned} \quad (20)$$

**Table 1**

The parameters for Entangled Network (EN) model and the Gent model

(a)	EN model	$G_c = 0.0378$ (MPa)	$N = 1133$	$G_e = 0.0695$ (MPa)
(b)	Gent model	$\mu = 0.0735$ (MPa)	$J_m = 3890$	

where  $\lambda$  is the stretch ratio. Thus, the phases velocities can be given explicitly as the function of the applied stretch ratio for the deformation modes. The general expressions for the shear waves propagating along  $\mathbf{n} = \cos \theta \mathbf{e}_1 + \sin \theta \mathbf{e}_2$  are given in Appendix B. For illustration, consider some special cases. For the shear waves propagating along  $\mathbf{n} = \mathbf{e}_3$ , the phase velocities  $c^{(1)}$  with  $\mathbf{m} = \mathbf{e}_1$  and  $c^{(2)}$  with  $\mathbf{m} = \mathbf{e}_2$ , corresponding to these deformation states are

$$\begin{aligned} c_u^{(1)} &= \sqrt{(9\lambda^{-1}\Theta_u^{-1}G_c + (\lambda + \lambda^{5/2})^{-1}G_e)/\rho_0} \quad \text{and} \\ c_u^{(2)} &= \sqrt{(9\lambda^{-1}\Theta_u^{-1}G_c + 0.5\lambda^{1/2}G_e)/\rho_0}, \end{aligned} \quad (21)$$

$$c_{eb}^{(1)} = c_{eb}^{(2)} = \sqrt{(9\lambda^{-4}\Theta_{eb}^{-1}G_c + (\lambda + \lambda^4)^{-1}G_e)/\rho_0}, \quad (22)$$

$$\begin{aligned} c_{ps}^{(1)} &= \sqrt{(9\lambda^{-2}\Theta_{ps}^{-1}G_c + (\lambda + \lambda^3)^{-1}G_e)/\rho_0} \quad \text{and} \\ c_{ps}^{(2)} &= \sqrt{(9\lambda^{-2}\Theta_{ps}^{-1}G_c + (1 + \lambda)^{-1}G_e)/\rho_0}. \end{aligned} \quad (23)$$

Note that in case of equi-biaxial deformation, equal wave velocities are obtained because of the symmetry of the deformation state in  $(\mathbf{e}_1, \mathbf{e}_2)$  plane.

For completeness, we compare our results for EN model with Gent model [58]. Recall that the Gent model considers the limiting extensibility of polymer chains only, while the EN model accounts for both the inter-molecular entanglements and the limited chain extensibility. The SEDF of the Gent model is

$$\psi_G = -\frac{1}{2}\mu J_m \ln \left( 1 - \frac{I_1 - 3}{J_m} \right) \quad (24)$$

where  $\mu$  is the initial shear modulus and  $J_m$  is the locking parameter. The corresponding acoustic tensor is

$$\hat{\mathbf{Q}}_G(\mathbf{F}, \mathbf{n}) = q_{G1} \hat{\mathbf{I}} + q_{G2} \hat{\mathbf{I}} \cdot (\mathbf{B} \cdot \mathbf{n} \otimes \mathbf{B} \cdot \mathbf{n}) \cdot \hat{\mathbf{I}} \quad (25)$$

where

$$q_{G1} = \mu J_m \Theta_G^{-1} (\mathbf{n} \cdot \mathbf{B} \cdot \mathbf{n}) \quad \text{and} \quad q_{G2} = 2\Theta_G^{-2} \mu J_m \quad (26)$$

where  $\Theta_G = 3 + J_m - I_1$ . The acoustic tensor  $\hat{\mathbf{Q}}_G$  has two non-trivial eigenvalues  $a_{G1}$  and  $a_{G2}$ , and the corresponding shear wave phase velocities are

$$c_G^{(1)} = \sqrt{a_{G1}^{(1)}/\rho_0} \quad \text{and} \quad c_G^{(2)} = \sqrt{a_{G2}^{(2)}/\rho_0}. \quad (27)$$

The explicit expression for Gent materials can be found in Galich and Rudykh [59], and the specification of the results for the deformation modes considered here are provided in Appendix C for completeness.

To compare the predictions of the two models, we first adopt the corresponding material parameters based on a set of available experimental data. In particular, we use the experimental data for silicone rubber subjected to uniaxial deformation [57]. Fig. 2 shows the comparison of the experimental data (black square symbols) and the modeling results (see red and blue solid curves) in terms of the first Piola-Kirchhoff stress component ( $P_{11}$ ) plotted versus the applied stretch ratio. To ensure both models produce identical phase velocities in the undeformed state, identical initial shear moduli for Gent and EN models are used. The moduli are  $\mu = G_c / [(1 - 1/N)(1 + 1/(2N))] + G_e/2 = \mu_0$ ; where  $\mu_0$  is the initial shear modulus of the silicone rubber. The fitting parameters for both material models are summarized in Table 1. Clearly, EN model accurately emulates the mechanical response of the silicone rubber, whereas Gent model fails to capture the material softening behavior under large

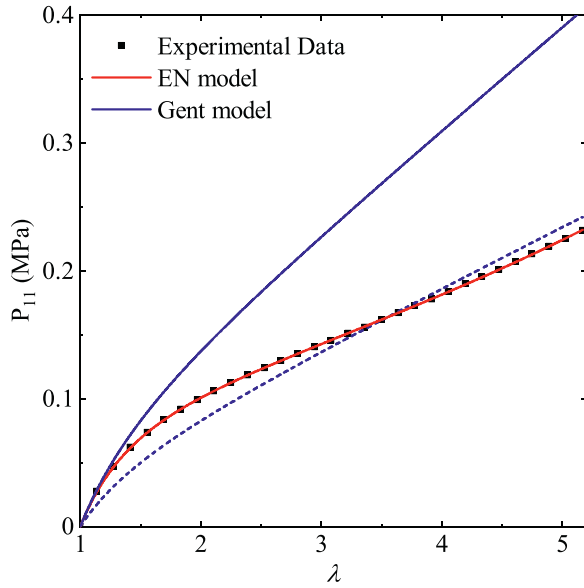


**Fig. 2.** The fitting results for Entangled Network (EN) and Gent model on the experimental data corresponding to uniaxial deformation of silicone rubber. The data is adapted from Xiang et al. [57].

deformation. More specifically, the relative error between the modeling results of Gent model and experimental data is higher than 50% for  $\lambda > 2.546$ . If the initial shear modulus constraint is relaxed, Gent model can capture the mechanical response over the considered deformation range (the corresponding fitting results for Gent model without the initial shear modulus constraint are denoted by the blue dashed curve in Fig. 2). This agreement, however, comes at the cost of significantly underestimated shear modulus in the undeformed state. In particular, the shear modulus is reduced by a factor of  $\approx 0.64$ . While it is a common approach in the stress-strain material characterization, this approach produces significant inaccuracies in the shear wave velocity values that do not agree with the classical results for the linear elasticity,  $c_0 = \sqrt{\mu_0/\rho_0}$ . Therefore, we use the constrained fitting results in our comparison of the model predictions.

In the following subsections, we will show the comparison of the shear wave velocities obtained for the two models with their parameters summarized in Table 1. In particular, we will examine the influence of (i) deformation and (ii) direction of propagation by making use of the derived expressions.

### 3.1. Effect of deformation on wave propagation in soft elastomers

In this subsection, we examine the dependence of shear wave characteristics on the deformation of soft elastomers. To this end, in Fig. 3 we plot the normalized phase velocities  $c/c_0$  as functions of stretch ratio. The results are shown for both models with their material parameters given in Table 1. We show the results for uniaxial (a), equi-biaxial (b), and pure shear (c) deformation modes. We consider the shear waves propagating in the direction  $\mathbf{n} = \mathbf{e}_3$  with polarizations  $\mathbf{m} = \mathbf{e}_1$  (dashed curves) and  $\mathbf{m} = \mathbf{e}_2$  (dotted curves). These phase velocities are governed by Eqs. (21)–(23). Recall that for the Gent model, equal phase velocities are obtained for both shear waves traveling in the direction  $\mathbf{n} = \mathbf{e}_3$  (see Eqs. (C.2)–(C.4)); the corresponding results of the Gent model denoted by the black solid curves are added for comparison.

The plots clearly indicate the significant influence of applied deformation on the phase velocities for both models. Recall that the elastomer experiences compression along the direction  $\mathbf{e}_3$  when subjected to tension ( $\ln(\lambda) > 0$ ) along  $\mathbf{e}_1$  and vice versa. Therefore, the velocities of shear waves propagating along this direction ( $\mathbf{n} = \mathbf{e}_3$ ) decrease with an increase in  $\lambda$ . This holds true for both models for the considered

deformation mode and polarizations of shear waves, with the exception of one scenario. This exceptional scenario corresponds to shear waves with  $\mathbf{m} = \mathbf{e}_2$  in EN material subjected to the uniaxial loading (see the dotted curve in Fig. 3 (a)). This case illustrates the competing mechanism between the crosslinked and entanglement terms in the governing equation (21). As the stretch ratio is increased, the crosslinked term contributed to decreasing the phase velocity, whereas the entanglement term contributes to increasing the phase velocity. Therefore, in the crosslinked part dominant region, we observe that the phase velocity decreases with an increase in  $\lambda$ ; however, after a certain stretch level ( $\lambda \approx 1.7$ ), the intermolecular entanglement start dominating, and the phase velocities start increasing. Accordingly, a further increase in  $\lambda$  results in an increase in the phase velocity.

As expected, both models predict equal value of phase velocities ( $c = c_0$ ) in the undeformed elastomer ( $\lambda = 1$ ). However, in the deformed state, the values of wave velocities predicted by the models differ. Moreover, the difference in their estimates increases with an increase in the applied deformation level. The disparity between the wave characteristics predictions of Gent and EN model can be attributed to the influence of entanglements on wave propagation in soft elastomers. The effect of entanglements varies with deformation modes. For example, in the case of uniaxial deformation, the velocity of the shear wave with  $\mathbf{m} = \mathbf{e}_1$  is higher (or lower) for EN model than Gent model, when  $\ln(\lambda) < 0$  (or  $\ln(\lambda) > 0$ ) (compare the dashed and solid curves in Fig. 3 (a)). For the equi-biaxial deformation mode, however, the phase velocities for the Gent model are higher (or lower) when the elastomer experiences tensile (or compressive) strains in the wave propagation direction (see Fig. 3 (b)). In contrast, under pure shear deformation, the velocity of the shear wave with  $\mathbf{m} = \mathbf{e}_1$  is always higher for the Gent model for both of tensile and compressive regimes (see Fig. 3 (c)).

We observe that for uniaxial and pure shear deformation modes, EN model predicts different phase velocities for waves with different polarizations. This difference in the velocities arises from the unequal deformation in the polarization direction ( $\mathbf{m} = \mathbf{e}_1$  and  $\mathbf{m} = \mathbf{e}_2$ ). In particular, the phase velocities of shear waves with  $\mathbf{m} = \mathbf{e}_1$  is higher than that of shear waves with  $\mathbf{m} = \mathbf{e}_2$  under tension in the direction of wave propagation, while opposite behavior is observed when  $\ln(\lambda) > 0$  (compare the dashed and dotted curves in Fig. 3 (a) and (c)). However, in the case of equi-biaxial deformation, the elastomer undergoes equal deformation along the  $\mathbf{e}_1$  and  $\mathbf{e}_2$  directions. Therefore, equal phase velocities are obtained for both polarizations (22). The shear wave velocity estimates of the Gent model do not depend on the polarization direction.

### 3.2. Effect of propagation direction on shear wave propagation in finitely deformed elastomers

Here, we study the effect of propagation direction on shear waves in finitely deformed elastomers. Recall that the shear waves traveling in the loading plane, i.e.,  $\mathbf{n} = \cos \theta \mathbf{e}_1 + \sin \theta \mathbf{e}_2$ , have two distinct phase velocities. These phase velocities strongly depend on angle  $\theta$ , with their expressions given by Eqs. (B.1)–(B.3) for EN model, and Eqs. (C.5)–(C.7) for Gent model. To illustrate the velocity dependence on angle  $\theta$ , we plot the polar diagrams for shear wave phase velocities traveling in  $(\mathbf{e}_1, \mathbf{e}_2)$  plane. We consider uniaxial ((a), (d)), equi-biaxial ((b), (e)), and pure shear ((c), (f)) deformation modes. The results are shown for EN (solid curves) and Gent (dashed curves) materials subjected to compression  $\lambda = 0.5$  (red curves) and tension  $\lambda = 3$  (blue curves); black curves denote the results for the undeformed state ( $\lambda = 1$ ). We illustrate the phase velocities for shear waves with out-of-plane polarization  $\mathbf{m} = \mathbf{e}_3$  (Fig. 4 (a)–(c)) and in-plane polarization  $\mathbf{m} = \sin \theta \mathbf{e}_1 - \cos \theta \mathbf{e}_2$  (Fig. 4 (d)–(f)).

In the undeformed state, as expected, the phase velocities are independent of propagation direction. Moreover, the wave velocities in elastomer subjected to equi-biaxial deformation are also independent of angle  $\theta$  (see Fig. 4 (b) and (e)), for both the EN (B.2) and Gent model (C.5). However, under the uniaxial and pure shear deformation modes, the shear wave velocities significantly depend on the direction of prop-



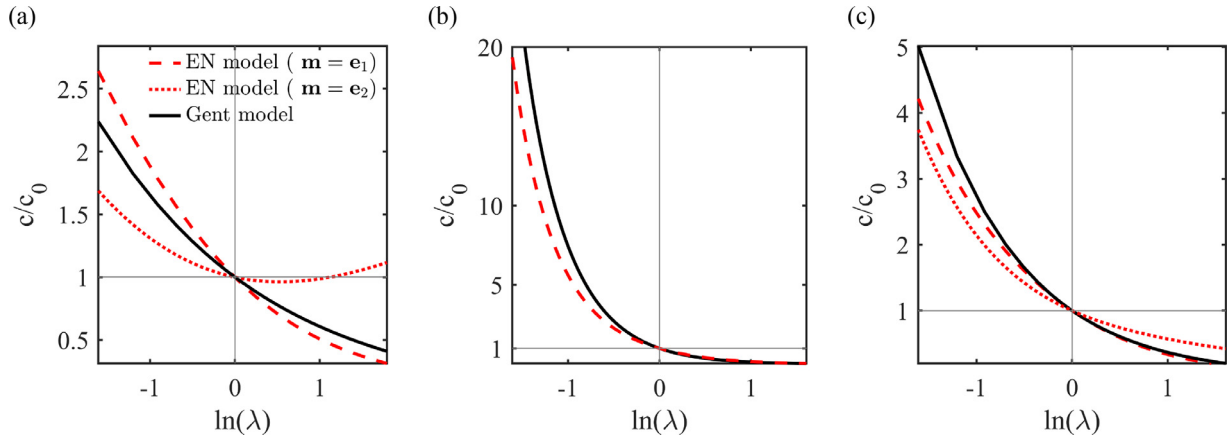


**Fig. 3.** The normalized phase velocities  $c/c_0$  vs  $\ln(\lambda)$  for the three deformation modes: (a) uniaxial, (b) equi-biaxial, and (c) pure shear. The phase velocities are shown for waves traveling in the direction  $\mathbf{n} = \mathbf{e}_3$  with polarizations  $\mathbf{m} = \mathbf{e}_1$  (dashed curves) and  $\mathbf{m} = \mathbf{e}_2$  (dotted curves). The results of Gent model are added for comparison (solid curves).

agation. We note that the maxima and minima of phase velocities are always found along either of the principal axes. This holds true regardless of the wave polarization. In particular, EN model produce the maximum and minimum phase velocities when the shear wave propagate in the direction with the largest tensile and compressive deformation, respectively.

For  $\lambda = 3$ , the highest tensile and compressive deformation levels are encountered by the waves traveling at  $\theta = 0$  ( $\mathbf{n} = \mathbf{e}_1$ ) and  $\theta = \pi/2$  ( $\mathbf{n} = \mathbf{e}_2$ ), respectively. Therefore, phase velocity monotonically decreases as the propagation direction angle varies from  $\theta = 0$  to  $\theta = \pi/2$  (see the blue curves in Fig. 4 (a), (c), (d) and (f)). For  $\lambda = 0.5$ , however, maxima and minima occurs in  $\mathbf{e}_2$  and  $\mathbf{e}_1$  directions, respectively (see red curves in Fig. 4 (a), (c), (d) and (f)).

Clearly, the two models predict different velocities, and the difference between their predictions significantly varies with propagation direction. For example, in the elastomers subjected to uniaxial and pure shear deformations with  $\lambda = 3$ , the phase velocity of shear waves with  $\mathbf{m} = \mathbf{e}_3$  predicted by EN model is higher than Gent model when the wave propagates along the compressive direction  $\theta = \pi/2$ , whereas it is higher for Gent model when propagating in tensile direction  $\theta = 0$  (see blue curves in Fig. 4 (a) and (c)). For the compression case of  $\lambda = 0.5$ , similar behavior is observed. In particular, the phase velocity of the waves propagating in the compressive (tensile) direction, predicted by EN model is higher (lower) than those predicted by the Gent model (see the red curves). We find that for the waves with in-plane polarization  $\mathbf{m} = \sin\theta\mathbf{e}_1 - \cos\theta\mathbf{e}_2$ , wave velocity predicted by Gent model are higher at all the angles when  $\lambda = 3$ , while for  $\lambda = 0.5$ , EN model estimates comparatively higher velocities (see Fig. 4 (d) and (f)).

These results clearly show the significant differences in the elastic wave characteristics predicted by the two models. The difference in the results can be attributed to the inter-molecular entanglements of polymer chains. We examine the influence of inter-molecular entanglements on the shear waves in the next subsection.

### 3.3. Effect of inter-molecular entanglements on shear wave propagation

Finally, we study the effect of inter-molecular entanglements on the shear wave characteristics. We consider the shear waves propagating along the direction  $\mathbf{n} = \mathbf{e}_3$ . To eliminate the effects of the limiting chain extensibility, we set the parameters  $J_m$  and  $N$  to infinity. Hence, Eqs. (21)–(23) reduce to

$$\begin{aligned} c_u^{(1)} &= \lambda^{-1/2} \sqrt{(G_c + G_e/(1 + \lambda^{3/2}))}/\rho_0 \quad \text{and} \\ c_u^{(2)} &= \lambda^{-1/2} \sqrt{(G_c + \lambda^{3/2}G_e)/\rho_0} \end{aligned} \quad (28)$$

$$c_{eb}^{(1)} = c_{eb}^{(2)} = \lambda^{-2} \sqrt{(G_c + G_e/(1 + \lambda^{-3}))}/\rho_0, \quad (29)$$

$$c_{ps}^{(1)} = \lambda^{-1} \sqrt{(G_c + G_e/(\lambda + \lambda^{-1}))}/\rho_0 \quad \text{and}$$

$$c_{ps}^{(2)} = \lambda^{-1} \sqrt{(G_c + G_e/(\lambda^{-2} + \lambda^{-1}))}/\rho_0 \quad (30)$$

and Eqs. (C.2)–(C.4) simplifies to the expressions corresponding to neo-Hookean material, namely,

$$c_{Gu}^{(1)} = c_{Gu}^{(2)} = \lambda^{-1/2} \sqrt{\mu/\rho_0}, \quad (31)$$

$$c_{Geb}^{(1)} = c_{Geb}^{(2)} = \lambda^{-2} \sqrt{\mu/\rho_0}, \quad (32)$$

$$c_{Gps}^{(1)} = c_{Gps}^{(2)} = \lambda^{-1} \sqrt{\mu/\rho_0}. \quad (33)$$

To ensure that both models produce identical results for the undeformed material, we maintain identical values for the initial shear moduli, i.e.,  $\mu = G_c + G_e/2$ . To quantify the extent of entanglements, we introduce the *entanglement strength* as the ratio  $G_e/G_c$ .

Fig. 5 shows the normalized phase velocity  $c/c_0$  (given by Eqs. (28)–(30)) as functions of the entanglement strength. The dashed and dotted curves correspond to the shear waves with polarizations  $\mathbf{m} = \mathbf{e}_1$  and  $\mathbf{m} = \mathbf{e}_2$ , respectively. The elastomer is subjected to uniaxial (Fig. 5 (a)), equi-biaxial (Fig. 5 (b)), and pure shear (Fig. 5 (c)) deformation modes with  $\lambda = 0.5$  (red curves) and  $\lambda = 3$  (blue curves); black curves denote the velocities in the undeformed elastomer. The phase velocities for Gent model (given by Eq. (31)–(33)) correspond to the case  $G_e/G_c = 0$ ; these values are marked by the horizontal solid lines in Fig. 5.

The phase velocities are independent of  $G_e/G_c$  in the undeformed elastomer. The entanglement strength, however, significantly affects the phase velocities in the deformed elastomer. Similar to the observations in Sec. 3.1, we find that the effect of entanglements on the wave characteristics varies with the wave's polarization and deformation modes. For example, under uniaxial tension ( $\lambda = 3$ ), the phase velocity corresponding to the shear waves with  $\mathbf{m} = \mathbf{e}_1$  decreases with an increase in entanglement strength, whereas for waves with polarization  $\mathbf{m} = \mathbf{e}_2$  the velocity increases (see blue curves in Fig. 5 (a)). However, a completely reverse trend is observed under uniaxial compression ( $\lambda = 0.5$ ) (see red curves).

For equi-biaxial deformation, identical wave velocities are obtained for both polarizations. Moreover, an increase in  $G_e/G_c$  leads to a decrease in these phase velocities under compression ( $\lambda = 0.5$ ), and leads to an increase when subjected to tension (see Fig. 5 (b)). Similar to the uniaxial deformation case, under pure shear deformation, unequal de-

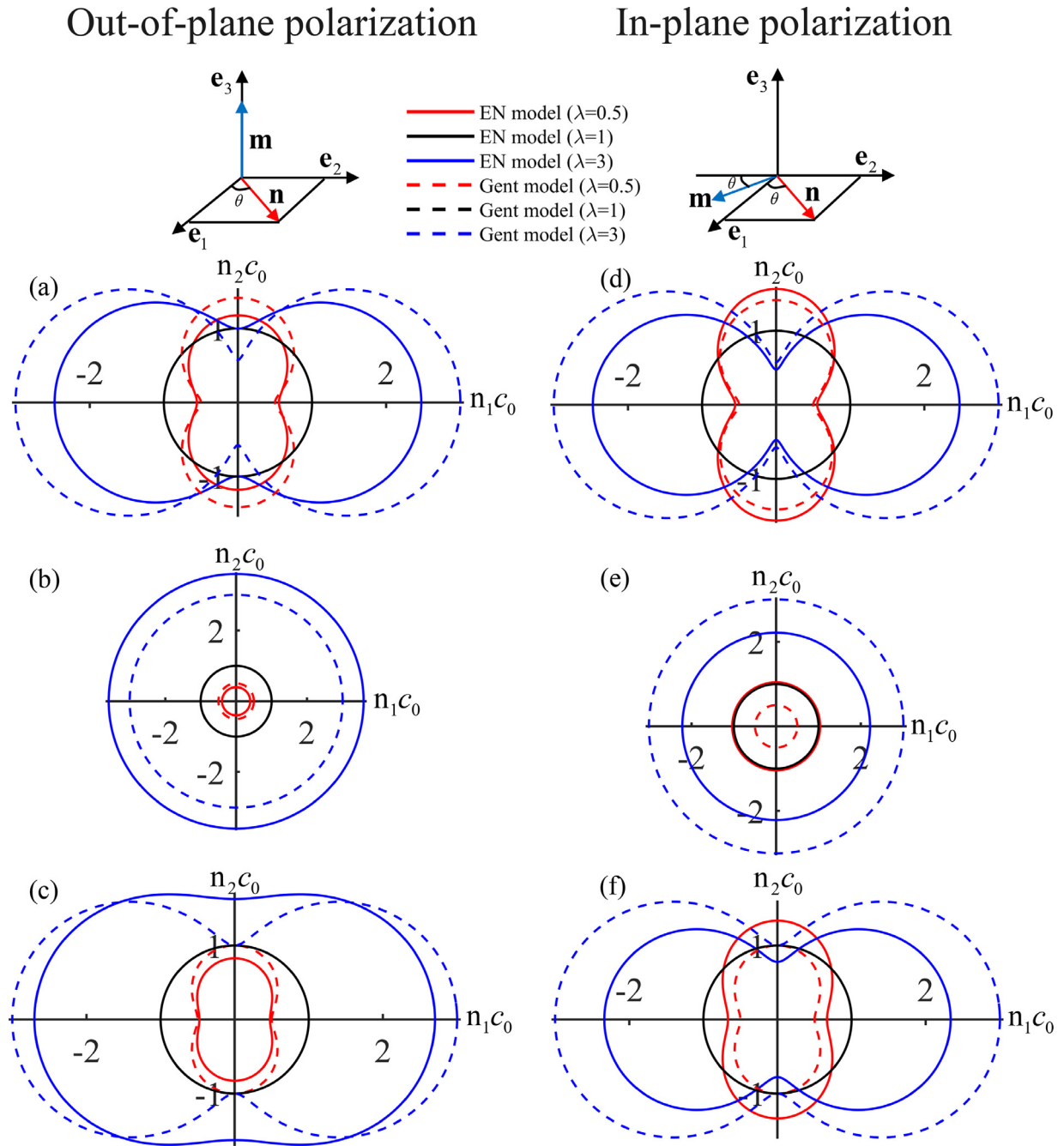


**Fig. 4.** The phase velocity polar diagrams for waves with polarizations: (a, b, c)  $\mathbf{m} = \mathbf{e}_3$  (out-of-plane) and (d, e, f)  $\mathbf{m} = \sin \theta \mathbf{e}_1 - \cos \theta \mathbf{e}_2$  (in-plane). Three deformation modes are considered: (a, d) uniaxial; (b, e) equi-biaxial; and (c, f) pure shear. The results for Gent model are added for comparison (dashed curves).

formation also takes place along the polarization directions,  $\mathbf{m} = \mathbf{e}_1$  and  $\mathbf{m} = \mathbf{e}_2$ ; this results in distinct phase velocities of the waves with those polarization. Moreover, the phase velocity corresponding to waves with  $\mathbf{m} = \mathbf{e}_1$  decreases with an increase in entanglement strength irrespective of compression or tension. However, the velocity of waves with polarization  $\mathbf{m} = \mathbf{e}_2$  increases with an increase in  $G_e/G_c$  for the tensile case ( $\lambda = 3$ ), and decreases for the compressive case ( $\lambda = 0.5$ ) (see dotted curves in Fig. 5 (c)).

#### 4. Elastic wave estimates for finitely deformed fiber composites with stiffening phases

In this section, we examine the shear wave propagation in *microstructured* hyperelastic fiber composites. In particular, we consider trans-

versely isotropic (TI) fiber composites with random distribution of fibers aligned along the direction  $\mathbf{L} \equiv \mathbf{e}_3$  (as shown in Fig. 6). Here and thereafter, the fields and parameters corresponding to the fiber and matrix phase are denoted as  $(\bullet)^{(f)}$  and  $(\bullet)^{(m)}$ , respectively. The volume fraction of fiber phase is  $v^{(f)}$  and that of the matrix phase is  $v^{(m)} = 1 - v^{(f)}$ . The macroscopic deformation gradient is defined as

$$\bar{\mathbf{F}} = \frac{1}{\mathfrak{V}_0} \int_{\mathfrak{V}_0} \mathbf{F}(\mathbf{X}) d\mathbf{X}, \quad (34)$$

where  $\mathfrak{V}_0$  is the volume occupied by the composite in the reference configuration. To capture the effect of stiffening behavior due to finite extensibility of the polymer chains, we employ the Gent model (24) to describe the behavior of the matrix and fiber phases.

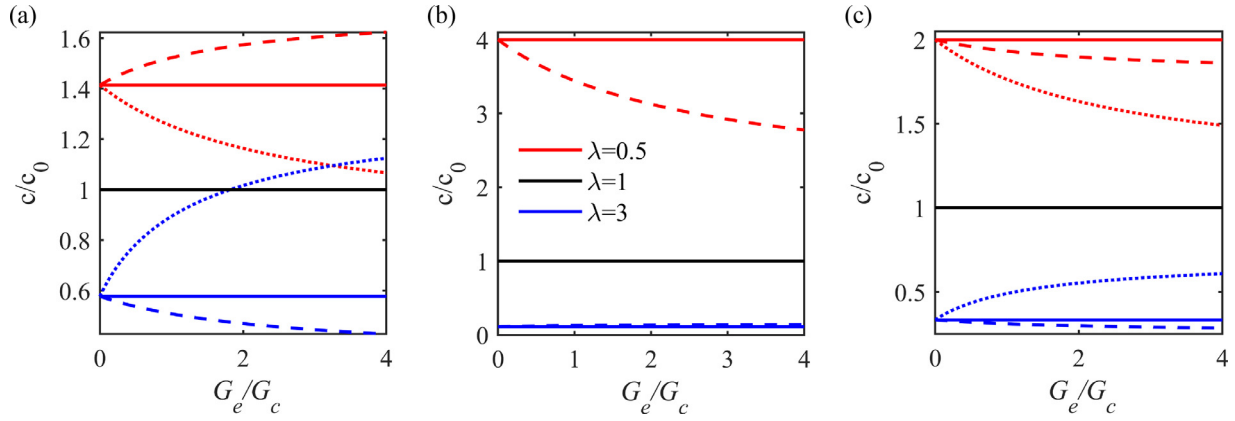


**Fig. 5.** Normalized shear wave velocities  $c/c_0$  as functions of entanglement strength  $G_e/G_c$ . The shear waves propagation direction is  $\mathbf{n} = \mathbf{e}_3$ , with polarizations  $\mathbf{m} = \mathbf{e}_1$  (dashed curve) and  $\mathbf{m} = \mathbf{e}_2$  (dotted curve). The horizontal solid lines denote the results for Gent model.

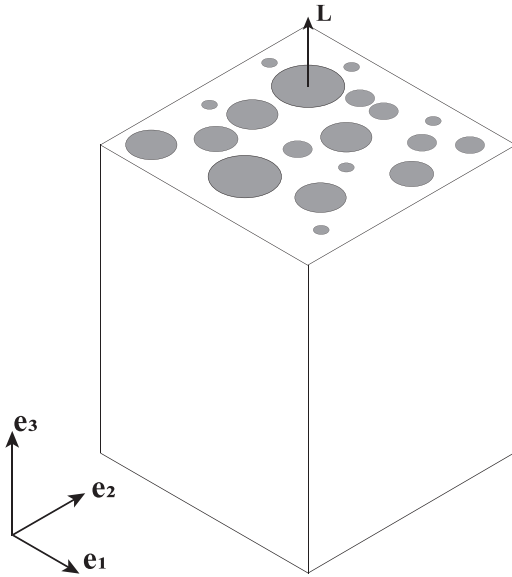


**Fig. 6.** Schematic representation of transversely isotropic fiber composite with random distribution of fibers, aligned along the direction  $\mathbf{L}$ .

For simplicity, we consider the FCs undergoing uniaxial deformation, hence, the macroscopic deformation gradient is

$$\bar{\mathbf{F}} = \bar{\lambda} \mathbf{e}_3 \otimes \mathbf{e}_3 + \bar{\lambda}^{-1/2} (\mathbf{I} - \mathbf{e}_3 \otimes \mathbf{e}_3), \quad (35)$$

where  $\bar{\lambda}$  is the applied macroscopic stretch ratio along the fiber direction. The effective behavior of the TI FCs with incompressible Gent phases under the uniaxial tension can be described using the following SEDF [60]

$$\bar{\psi}(\bar{\mathbf{F}}) = -\frac{1}{2} \left[ v^{(m)} \mu^{(m)} J_m^{(m)} \ln \left( 1 - \frac{\bar{I}_1^{(m)} - 3}{J_m^{(m)}} \right) + v^{(f)} \mu^{(f)} J_m^{(f)} \ln \left( 1 - \frac{\bar{I}_1^{(f)} - 3}{J_m^{(f)}} \right) \right], \quad (36)$$

where

$$\bar{I}_1^{(r)} = \bar{I}_4 + 2\bar{I}_4^{-1/2} + \alpha^{(r)} \left( \bar{I}_1 - \bar{I}_4 - 2\bar{I}_4^{-1/2} \right), \quad (37)$$

with

$$\alpha^{(f)} = \left( 1 - v^{(m)} \frac{G^{(f)} - G^{(m)}}{G^{(f)} v^{(m)} + G^{(m)} (1 + v^{(f)})} \right)^2 \quad (38)$$

and

$$\alpha^{(m)} = \left( 1 + v^{(f)} \frac{G^{(f)} - G^{(m)}}{G^{(f)} v^{(m)} + G^{(m)} (1 + v^{(f)})} \right)^2 + v^{(f)} \left( \frac{G^{(f)} - G^{(m)}}{G^{(f)} v^{(m)} + G^{(m)} (1 + v^{(f)})} \right)^2; \quad (39)$$

here  $G^{(r)} = J_m^{(r)} \mu^{(r)} / \gamma^{(r)}$  is the phase effective shear modulus, with  $\gamma^{(r)} = J_m^{(r)} - (\bar{I}_1 - 3)$ ;  $\bar{I}_1 = \text{tr} \bar{\mathbf{C}}$ ,  $\bar{I}_4 = \mathbf{L} \cdot \bar{\mathbf{C}} \cdot \mathbf{L}$ ;  $\bar{\mathbf{C}} = \bar{\mathbf{F}}^T \bar{\mathbf{F}}$  is the average right Cauchy-Green deformation tensor.<sup>2</sup> We note that, in small strain limit, the effective behavior of incompressible hyperelastic FCs described by Eq. (36) is in agreement with the mathematical results for linear elastic FCs [61].

The acoustic tensor (11) corresponding to the effective SEDF (36) takes the form

$$\mathbf{Q}(\mathbf{n}) = \bar{q}_1 \mathbf{I} + \bar{q}_2 (\bar{\mathbf{B}} \cdot \mathbf{n}) \otimes (\bar{\mathbf{B}} \cdot \mathbf{n}) + \bar{q}_3 [(\bar{\mathbf{B}} \cdot \mathbf{n}) \otimes (\bar{\mathbf{F}} \cdot \mathbf{L}) + (\bar{\mathbf{F}} \cdot \mathbf{L}) \otimes (\bar{\mathbf{B}} \cdot \mathbf{n})] + \bar{q}_4 (\bar{\mathbf{F}} \cdot \mathbf{L}) \otimes (\bar{\mathbf{F}} \cdot \mathbf{L}), \quad (40)$$

where  $\bar{\mathbf{B}} = \bar{\mathbf{F}} \bar{\mathbf{F}}^T$  is the average left Cauchy-Green deformation tensor; and

$$\begin{aligned} \bar{q}_1 &= \bar{G}(\mathbf{n} \cdot \bar{\mathbf{B}} \cdot \mathbf{n}) + (\bar{G} - \bar{G})(1 - \bar{\lambda}^{-3})(\mathbf{n} \cdot \bar{\mathbf{F}} \cdot \mathbf{L})^2, \\ \bar{q}_2 &= 2\beta, \\ \bar{q}_3 &= 2\zeta(1 - \bar{\lambda}^{-3})(\mathbf{n} \cdot \bar{\mathbf{F}} \cdot \mathbf{L}), \quad \text{and} \\ \bar{q}_4 &= [3(\bar{G} - \bar{G})\bar{\lambda}^{-5} + 2\eta(1 - \bar{\lambda}^{-3})^2](\mathbf{n} \cdot \bar{\mathbf{F}} \cdot \mathbf{L})^2. \end{aligned} \quad (41)$$

with

$$\begin{aligned} \beta &= v^{(m)} G^{(m)} \alpha^{(m)2} / \gamma^{(m)} + v^{(f)} G^{(f)} \alpha^{(f)2} / \gamma^{(f)}, \\ \zeta &= v^{(m)} G^{(m)} \alpha^{(m)} (1 - \alpha^{(m)}) / \gamma^{(m)} + v^{(f)} G^{(f)} \alpha^{(f)} (1 - \alpha^{(f)}) / \gamma^{(f)}, \quad \text{and} \\ \eta &= v^{(m)} G^{(m)} (1 - \alpha^{(m)})^2 / \gamma^{(m)} + v^{(f)} G^{(f)} (1 - \alpha^{(f)})^2 / \gamma^{(f)}. \end{aligned} \quad (42)$$

The effective moduli  $\bar{G}$  and  $\bar{G}$  are

$$\bar{G} = G^{(m)} \frac{(1 + v^{(f)})G^{(f)} + v^{(m)}G^{(m)}}{v^{(m)}G^{(f)} + (1 + v^{(f)})G^{(m)}} \quad \text{and} \quad \bar{G} = v^{(f)}G^{(f)} + v^{(m)}G^{(m)}. \quad (43)$$

The acoustic tensor  $\hat{\mathbf{Q}}$  given in Eq. (40) has two non-trivial eigenvalues:  $\bar{a}_1$  and  $\bar{a}_2$ , with the eigenvectors lying in the plane perpendicular to  $\mathbf{n}$ . Hence, we have two distinct shear waves with the corresponding phase velocities

$$\bar{c}_{sw}^{(1)} = \sqrt{\bar{a}_1 / \bar{\rho}_0} \quad \text{and} \quad \bar{c}_{sw}^{(2)} = \sqrt{\bar{a}_2 / \bar{\rho}_0}, \quad (44)$$

where  $\bar{\rho}_0 = v^{(f)} \rho_0^{(f)} + v^{(m)} \rho_0^{(m)}$  is the average initial density of the composite.

<sup>2</sup> Note that  $\bar{I}_1 = \text{tr} \bar{\mathbf{C}} = \text{tr} \bar{\mathbf{B}}$  and  $\bar{I}_4 = \mathbf{L} \cdot \bar{\mathbf{C}} \cdot \mathbf{L} = \mathbf{L} \cdot \bar{\mathbf{B}} \cdot \mathbf{L}$ ;  $\bar{\mathbf{B}} = \bar{\mathbf{F}} \bar{\mathbf{F}}^T$  is the average left Cauchy-Green deformation tensor.

While, in general, the two shear wave velocities are distinct, they do coincide for some propagation directions. For example, the shear waves propagating perpendicular to the direction of fibers,  $\mathbf{n} \perp \mathbf{L}$ , so that  $\mathbf{n} = \cos \theta \mathbf{e}_1 + \sin \theta \mathbf{e}_2$ , are characterized by identical phase velocities, namely

$$\bar{c}_{sw}^{(1)} = \bar{c}_{sw}^{(2)} = \sqrt{\bar{\lambda}^{-1} \bar{G} / \bar{\rho}_0}. \quad (45)$$

Moreover, the velocities are independent of the angle  $\theta$ .

For shear waves propagating along the fiber direction ( $\mathbf{n} = \mathbf{L} = \mathbf{e}_3$ ), the phase velocities also coincide

$$\bar{c}_{sw}^{(1)} = \bar{c}_{sw}^{(2)} = \bar{\lambda} \sqrt{(\bar{G} + (\bar{G} - \bar{G})\bar{\lambda}^{-3}) / \bar{\rho}_0}, \quad (46)$$

as the corresponding elastic moduli tensor components of fiber composites are equal, specifically,  $A_{1313} = A_{2323}$ .

However, for the oblique shear waves ( $\mathbf{n} = \cos \phi \mathbf{e}_2 + \sin \phi \mathbf{e}_3$ ), two distinct phase velocities are obtained

$$\bar{c}_{sw}^{(1)} = \sqrt{\frac{\bar{G} + \sin^2(\phi) \bar{G}(\bar{\lambda}^3 - 1)}{\bar{\lambda} \bar{\rho}_0}}, \quad (\mathbf{m} = \mathbf{e}_1), \quad (47)$$

and

$$\bar{c}_{sw}^{(2)} = \sqrt{\frac{2 \sin^2(\phi) \cos^2(\phi) \bar{\Gamma}(\bar{\lambda}^3 - 1)^2 + \bar{\lambda}(\bar{G} + 3(\bar{G} - \bar{G}) \sin^4(\phi) + (\bar{G}(2 + \bar{\lambda}^3) - 3\bar{G}) \sin^2(\phi))}{\bar{\lambda}^2 \bar{\rho}_0}}, \quad (\mathbf{m} = -\sin \phi \mathbf{e}_2 + \cos \phi \mathbf{e}_3), \quad (48)$$

where

$$\bar{\Gamma} = \frac{\nu^{(m)} \bar{G}^{(m)}}{\gamma^{(m)}} + \frac{\nu^{(f)} \bar{G}^{(f)}}{\gamma^{(f)}}. \quad (49)$$

Clearly, expressions (47) and (48) produce identical values only at  $\phi = 0$  ( $\mathbf{n} = \mathbf{e}_2$ ), and at  $\phi = \pi/2$  ( $\mathbf{n} = \mathbf{e}_3$ ). The expressions (47) and (48) reduce to Eq. (45) for  $\phi = 0$ , and to Eq. (46) for  $\phi = \pi/2$ . For other directions ( $\phi \neq 0, \pi/2$ ), two distinct phase velocities exist. For instance, for  $\phi = \pi/4$ , these phase velocities are

$$\bar{c}_{sw}^{(1)} = \sqrt{\frac{2\bar{G} + \bar{G}(\bar{\lambda}^3 - 1)}{2\bar{\lambda} \bar{\rho}_0}}, \quad \mathbf{m} = \mathbf{e}_1 \quad (50)$$

and

$$\bar{c}_{sw}^{(2)} = \sqrt{\frac{2\bar{\Gamma}(\bar{\lambda}^3 - 1)^2 + \bar{G}(2\bar{\lambda}^4 + \bar{\lambda}) + \bar{G}\bar{\lambda}}{4\bar{\lambda}^2 \bar{\rho}_0}}, \quad \mathbf{m} = \frac{(\mathbf{e}_3 - \mathbf{e}_2)}{\sqrt{2}}. \quad (51)$$

We note that Eq. (46) yields an explicit expression for critical stretch corresponding to the onset of macroscopic instability in the TI FCs with Gent phases [60], namely,

$$\bar{\lambda}_{cr} = \left(1 - \frac{\bar{G}}{\bar{G}}\right)^{1/3}. \quad (52)$$

In the next subsection, we will make use of the derived analytical expressions to illustrate the effect of composite microstructure parameters – volume fraction of the constituents and initial shear modulus contrast – on the shear wave propagation in the FCs with Gent phases.

#### 4.1. Effect of microstructure parameters on wave propagation in FCs

Fig. 7 shows the phase velocities of the shear waves traveling along the direction of fibers as functions of fiber volume fraction  $\nu^{(f)}$  (a) and initial shear modulus contrast  $\mu^{(f)}/\mu^{(m)}$  (b). The phase velocities are calculated using the expression (46). The value of initial shear modulus contrast is  $\mu^{(f)}/\mu^{(m)} = 10$  in Fig. 7 (a), and fiber volume fraction is  $\nu^{(f)} = 0.2$  in Fig. 7 (b). The results are shown for the FCs with (i) Gent fibers with  $J_m^{(f)} = 0.1$  and neo-Hookean matrix (green dashed curves); (ii) with neo-Hookean fibers and Gent matrix with  $J_m^{(m)} = 0.1$  (red dotted curves); and (iii) with all-Gent phases with  $J_m^{(f)} = J_m^{(m)} = 0.1$  (blue dash-dotted curves). For comparison, the curves corresponding to neo-Hookean FC

are also included (black curves). We consider the FCs with identical densities for phases  $\rho_0^{(f)} = \rho_0^{(m)}$ . The FCs are subjected the macroscopic deformation level of  $\bar{\lambda} = 1.15$ . The phase velocities are normalized by the factor of  $\bar{c}_0 = \sqrt{\mu^{(m)}/\rho_0^{(m)}}$ .

As expected, the phase velocities increase for all the FCs, with an increase in fiber volume fraction (see Fig. 7 (a)). This increase occurs regardless of their material properties. In FCs with a given volume fraction, the value of the phase velocities depends on the phase stiffening characteristics (along with the deformation level). In FCs with either or both of the phases with stiffening behavior, the wave velocities are higher than the ones in the corresponding neo-Hookean composites; this is regardless of fiber volume fraction. Moreover, shear waves travel at higher speeds in all-Gent (or Gent-Gent) FCs as compared to other FCs at the same deformation level (see, for example, the blue curve in Fig. 7 (a)). This happens because stiffening of both phases contribute together in increasing the effective stiffness of the composite. We observe that at  $\nu^{(f)} = 0$ , the phase velocities of FCs with Gent matrix ( $J_m^{(m)} = 0.1$ ) and all-Gent phases ( $J_m = 0.1$ ) are identical. Also, FCs with Gent fibers and neo-Hookean phases have equal wave velocities. Moreover, the magnitude of the former pair is higher than the later one. This is because, at  $\nu^{(f)} = 0$ , the matrix phase is the only constituent, and therefore, the wave velocities are dictated by the matrix phase behavior. In particular, the lowest and highest velocity magnitudes correspond to the neo-Hookean and Gent ( $J_m^{(m)} = 0.1$ ) matrix phase, respectively. Similarly, at  $\nu^{(f)} = 1$ , fiber phase is the only constitutive material. Hence, for this homogeneous case, the wave velocities depend on the fiber phase behavior. We also find that the curves corresponding to the composites with Gent fibers  $J_m^{(f)} = 0.1$ , neo-Hookean matrix and neo-Hookean fibers, Gent matrix  $J_m^{(m)} = 0.1$  intersect at  $\nu^{(f)} \approx 0.3$  (see red and green curves in Fig. 7 (a)). In particular, for  $\nu^{(f)} < 0.3$ , the magnitude of wave velocities is higher in nH-Gent ( $J_m^{(m)} = 0.1$ ) FC than Gent-nH ( $J_m^{(f)} = 0.1$ ) FC. Whereas, at higher values of fiber volume fraction,  $\nu^{(f)} > 0.3$ , an opposite trend is observed.

The phase velocities increase with an increase in the shear modulus contrast. This is regardless of the material properties of phases (see Fig. 7 (b)). We also observe that the difference between the phase velocities of all-Gent and Gent-nH FCs decreases as the shear modulus contrast increases. Moreover, the curves corresponding to the velocities in neo-Hookean FC and nH-Gent FC approach each other for large value of the contrast  $\mu^{(f)}/\mu^{(m)}$ . However, the gap between the velocity magnitudes of all-Gent and neo-Hookean FCs consistently increases with an increase in the initial shear modulus contrast.

The results in Fig. 7 indicate that the phase stiffening significantly influences the shear wave propagation in FCs. In the following subsections, we investigate this influence in detail by explicitly studying the effects of (i) deformation, (ii) limiting extensibility of phases, and (iii) directionality of shear wave propagation in Gent FCs. We illustrate these effects by the examples of FCs with fiber volume fraction  $\nu^{(f)} = 0.2$  and initial shear modulus contrast  $\mu^{(f)}/\mu^{(m)} = 10$ .

#### 4.2. Effect of deformation on wave propagation in FCs

In this subsection, we study the effect of deformation on shear wave propagation in Gent FCs subjected to uniaxial deformation (35). Fig. 8 shows the phase velocities as functions of applied macroscopic stretch ratio  $\bar{\lambda}$ . In particular, we consider the shear waves traveling parallel (Fig. 8 (a)) and perpendicular (Fig. 8 (b)) to the fiber direction. These phase velocities are governed by the Eqs. (46) and (45), respectively. The results are shown for FCs with fiber volume fraction  $\nu^{(f)} = 0.2$  and initial shear modulus contrast  $\mu^{(f)}/\mu^{(m)} = 10$ . Similar to the previous consideration in Sec. 4.1, we examine the three morphologies of FCs with different phase stiffening characteristics, and neo-Hookean FC for comparison. The vertical thin dashed lines indicate the lock-up stretch values for Gent material with  $J_m = 0.1$ :  $\lambda_{lock-up} = 0.83$  (compression) and  $\lambda_{lock-up} = 1.19$  (tension). The phase velocities are normalized by



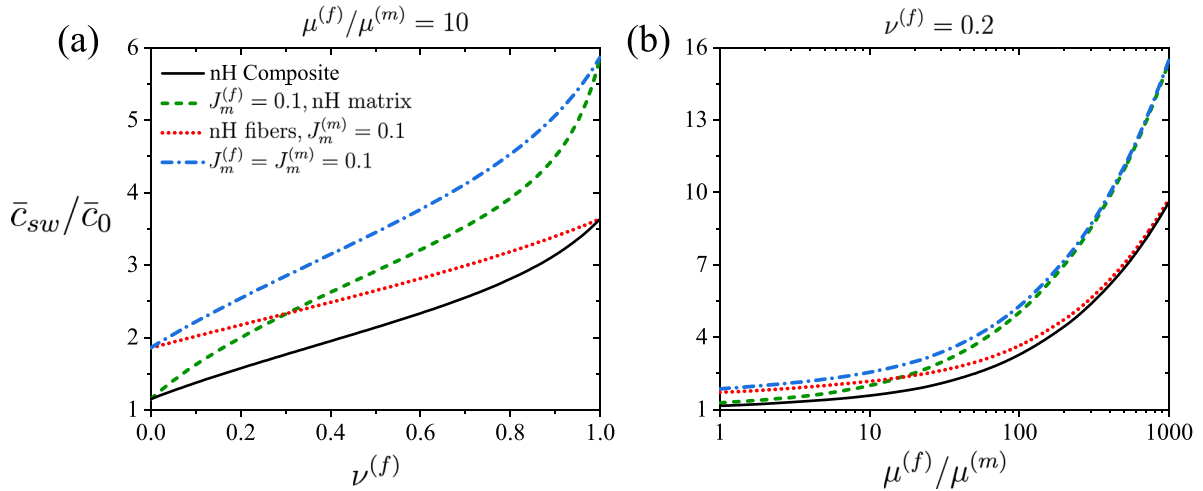


**Fig. 7.** Normalized phase velocities  $\bar{c}_{sw}/\bar{c}_0$  of shear waves traveling parallel to the fibers as the functions of (a) fiber volume fraction  $\nu^{(f)}$ , and (b) initial shear modulus contrast  $\mu^{(f)}/\mu^{(m)}$ . FCs with initial shear modulus contrast  $\mu^{(f)}/\mu^{(m)} = 10$  (a) and fiber volume fraction  $\nu^{(f)} = 0.2$  (b) are subjected to uniaxial tension,  $\bar{\lambda} = 1.15$ . The normalization factor is  $\bar{c}_0 = \sqrt{\mu^{(m)}/\rho_0^{(m)}}$ .

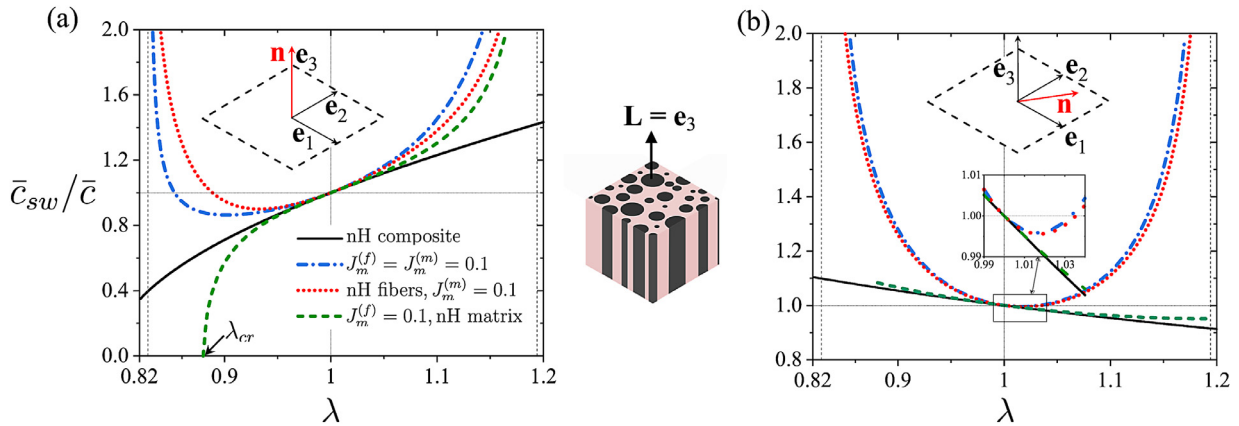


**Fig. 8.** Normalized phase velocities  $\bar{c}_{sw}/\bar{c}$  of shear waves traveling parallel (a), and perpendicular (b) to the fibers as the functions of stretch ratio  $\bar{\lambda}$ . FCs are considered with fiber volume fraction  $\nu^{(f)} = 0.2$  and initial shear modulus contrast  $\mu^{(f)}/\mu^{(m)} = 10$ .

$\bar{c} = \sqrt{\bar{\mu}/\bar{\rho}_0}$ , where

$$\bar{\mu} = \mu^{(m)} \frac{(1 + \nu^{(f)})\mu^{(f)} + \nu^{(m)}\mu^{(m)}}{\nu^{(m)}\mu^{(f)} + (1 + \nu^{(f)})\mu^{(m)}}. \quad (53)$$

We observe that in the small deformation range (strain  $\approx \pm 3\%$ ), the phase velocities of the shear waves in Gent FCs with the propagation direction  $\mathbf{n} = \mathbf{L}$  are barely different from those in the neo-Hookean FCs (see Fig. 8 (a)). At higher deformation levels, however, the effect of the phase stiffening becomes more prominent. In particular, in contrast to the neo-Hookean FCs (which show a consistent decrease in wave velocities under contraction), we do not observe a monotonous decrease in composites with Gent matrix and all-Gent phases (see red and blue curves in Fig. 8 (a)). In these Gent composites, the phase velocities decrease only up to their certain compressive strain levels. At higher compressive strains, the shear wave velocities start increasing with a further contraction along the fibers, as these composites experience stiffening of phase(s) at larger deformation levels. Therefore, even in the case of extension, these FCs show a comparatively larger increase in the wave velocities than the neo-Hookean FCs, when deformation approaches the locking limit  $\lambda_{lock-up}$  (see blue and red curves in Fig. 8(a)).

In a similar manner, the shear wave velocities significantly increase with  $\bar{\lambda}$  in composites with Gent FCs subjected to tensile loadings. However, in contrast to FCs with Gent matrix and all-Gent phases, the phase

velocities in FCs with Gent fibers monotonously decrease with a decrease in  $\bar{\lambda}$ , under compressive loadings (see green dashed curve in Fig. 8(a)). Moreover, the shear wave velocity attains zero value at a certain stretch ratio. This stretch ratio is referred to as the critical stretch ratio,  $\bar{\lambda}_{cr}$ , and it indicates the onset of macroscopic instability [62]. For the FCs considered in Fig. 8(a), with Gent fibers  $J_m^{(f)} = 0.1$  and neo-Hookean matrix, the critical stretch ratio is  $\bar{\lambda}_{cr} = 0.88$  (marked as “ $\bar{\lambda}_{cr}$ ”).

In FCs with Gent matrix and all-Gent phases, the stiffening of phase(s) also dictates the wave propagation perpendicular to the fibers ( $\mathbf{n} \perp \mathbf{L}$ ), at higher deformation levels. In particular, the wave velocity in these composites decreases with an increase in  $\bar{\lambda}$  only up to a certain value of tensile strain (see the inset in Fig. 8(b)). Under higher tensile strains, however, these composites show an increase in the wave velocity with an increase in deformation level (see the blue and red curves). Here, the influence of fiber phase stiffening on the wave velocities is rather weak (see the green dashed curve in Fig. 8(b)). We observe that the values of the shear wave velocities are close to those in the neo-Hookean FCs, even for  $\bar{\lambda}$  approaching the locking deformation level,  $\lambda_{lock-up}$ .

#### 4.3. Effect of phases' finite extensibility on wave propagation in FCs

Next, we study the effect of phase stiffening on the shear wave phase velocities in the TI FCs. Fig. 9 shows the velocity as a func-

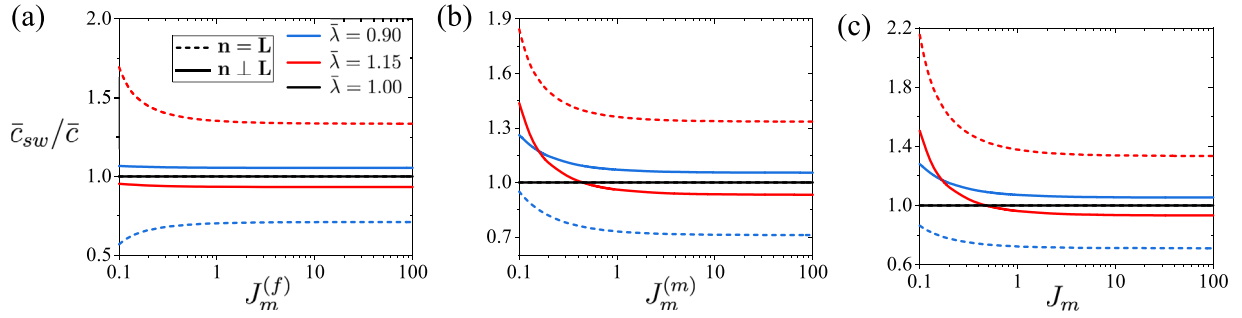


**Fig. 9.** Normalized phase velocities  $\bar{c}_{sw}/\bar{c}$  of shear waves as the functions of: fiber locking parameter  $J_m^{(f)}$  (a); matrix locking parameter  $J_m^{(m)}$  (b); and  $J_m = J_m^{(f)} = J_m^{(m)}$  (c). The dashed and solid curves correspond to the shear waves traveling parallel and perpendicular to the fibers, respectively. The fiber volume fraction is  $v^{(f)} = 0.2$  and initial shear modulus contrast is  $\mu^{(f)}/\mu^{(m)} = 10$ .

tion of the phase locking parameters for the FCs with (a) Gent fibers and neo-Hookean matrix, (b) neo-Hookean fibers and Gent matrix, and (c) both Gent phases with identical locking parameters  $J_m = J_m^{(f)} = J_m^{(m)}$  (Fig. 9(c)). The results are shown for the shear waves traveling in the direction perpendicular (solid curves) and parallel (dashed curves) to the fibers. The FCs are subjected to the uniaxial compression of  $\bar{\lambda} = 0.90$  (blue curves) and tension of  $\bar{\lambda} = 1.15$  (red curves). For comparison, the results for the undeformed FCs ( $\bar{\lambda} = 1$ ) are included as horizontal black lines. Note that all the FC morphologies in Fig. 9 are macroscopically stable for the considered deformation range.

In the undeformed FCs ( $\bar{\lambda} = 1$ ), the phase velocities are indeed independent of the phase locking parameters (see the horizontal black lines in Fig. 9). In the deformed FCs, however, the stiffening behavior of the phases significantly influences the shear wave propagation. In particular, we observe that in the composites with Gent matrix and neo-Hookean fibers, a decrease in the matrix locking parameter  $J_m^{(m)}$  leads to an increase in phase velocities. This happens for both tension or compression deformations (see Fig. 9(b)). Similarly, in FCs with all-Gent phases, the phase velocities increase with a decrease in  $J_m = J_m^{(f)} = J_m^{(m)}$ , for both propagation directions – perpendicular and parallel to the fibers (see Fig. 9(c)). In contrast, in composites with Gent fibers and neo-Hookean matrix, the stiffening of fibers only affects the phase velocities of waves traveling along the direction of fibers ( $\mathbf{n} = \mathbf{L}$ ). However, the stiffening effect of fiber phase is weak for the waves with  $\mathbf{n} \perp \mathbf{L}$ . Moreover, the influence of fiber locking parameter  $J_m^{(f)}$  is different in the compression and tension cases. In particular, the wave velocity for  $\mathbf{n} = \mathbf{L}$  decreases with an increase in  $J_m^{(f)}$  in the FCs under tension  $\bar{\lambda} = 1.15$  (see the dashed red curves in Fig. 9(a)), whereas the opposite behavior is observed for compressed FCs with  $\bar{\lambda} = 0.90$  (see the dashed blue curves in Fig. 9(a)). Furthermore, we note that at higher values of locking parameters, the phase velocities approach the values corresponding to the TI FCs with neo-Hookean phases, for each deformation level.

#### 4.4. Effect of propagation direction on shear wave velocity in FCs

Finally, we illustrate how the propagation direction affects the phase velocities of the shear waves in the TI FCs with Gent phases. Recall that the shear waves traveling in the plane perpendicular to the fibers, i.e.,  $\langle \mathbf{e}_1, \mathbf{e}_2 \rangle$  plane with  $\mathbf{n} = \cos \theta \mathbf{e}_1 + \sin \theta \mathbf{e}_2$ , have identical phase velocities and are independent of angle  $\theta$ . These velocities are given by Eq. (45).

However, the shear waves traveling at an oblique angle to the fibers, for example,  $\mathbf{n} = \cos \phi \mathbf{e}_2 + \sin \phi \mathbf{e}_3$ , have two distinct phase velocities. These velocities are given by Eq. (47) and Eq. (48) showing their strong dependence on angle  $\phi$ . To illustrate the velocity dependence on angle  $\phi$ , we plot the polar diagrams for the slowness  $\bar{s}_{sw}(\phi) = 1/\bar{c}_{sw}(\phi)$  for the waves traveling in  $\langle \mathbf{e}_2, \mathbf{e}_3 \rangle$  plane. The slowness curves are shown for shear waves with two polarizations:  $\mathbf{m} = \mathbf{e}_1$  (out-of-plane, Fig. 10(a) and (b)) and  $\mathbf{m} = -\sin \phi \mathbf{e}_2 + \cos \phi \mathbf{e}_3$  (in-plane, Fig. 10(c) and (d)). The results are shown for the FCs with (i) neo-Hookean phases (solid curves), (ii)

Gent fibers ( $J_m^{(f)} = 0.1$ ) and neo-Hookean matrix (dotted curve), and (iii) neo-Hookean fibers and Gent matrix ( $J_m^{(m)} = 0.1$ ) (dash-dotted curves). The FCs are subjected to uniaxial compression of  $\bar{\lambda} = 0.90$  (blue curves) and tension of  $\bar{\lambda} = 1.15$  (red curves); the results for the undeformed FCs ( $\bar{\lambda} = 1$ ) are denoted by the black curves.

We observe that for the *out-of-plane* shear waves, the maximum of phase velocities always lies in either of the principal directions, regardless of phase properties and deformation. In particular, when the FC is subjected to compressive loading, the maximum phase velocity is obtained along the direction  $\mathbf{n} = \mathbf{e}_2$  among all the directions in  $\langle \mathbf{e}_2, \mathbf{e}_3 \rangle$  plane (see Fig. 10(a)). Whereas in the case of tension, the maximum lies along the direction of propagation  $\mathbf{n} = \mathbf{e}_3$  (see Fig. 10(b)). In contrast, the maximum phase velocity for *in-plane* shear waves does not lie at the principal axes. Moreover, the directions along which the wave travels at the maximum speed ( $\mathbf{n}_{max} = \cos \phi_0 \mathbf{e}_2 + \sin \phi_0 \mathbf{e}_3$ ), depend on the combination of the phase properties and deformation level. The corresponding  $\phi_0$  can be explicitly expressed as

$$\phi_0 = \pm \frac{1}{2} \cos^{-1} \left( \frac{\bar{\lambda} \bar{G} (\bar{\lambda}^3 - 1)}{2(\bar{\lambda}^3 - 1)^2 \bar{\Gamma} + 3(\bar{G} - \bar{\Gamma}) \bar{\lambda}} \right) + \pi n, n = 0, 1. \quad (54)$$

In the undeformed FCs, the wave velocity maxima lies in the direction  $\mathbf{n} = (\mathbf{e}_2 \pm \mathbf{e}_3)/\sqrt{2}$ .

## 5. Conclusions

In this paper, we have analyzed elastic wave propagation in soft microstructured materials. We have studied the effects arising at different length-scales – from underlying molecular chain network mechanisms to the micromechanics of hyperelastic heterogeneous composites.

First, we examine the interplay between the crosslinked and entangled polymer chains and elastic wave characteristics in finitely deformed homogeneous materials. We have derived explicit expressions for phase velocity, and illustrated the influence of the inter-molecular entanglements on the wave propagation for various deformation states uniaxial, equi-biaxial, and pure shear. In addition, we compared these derived results with the Gent material model (a commonly used non-Gaussian hyperelastic model). The comparison was based on the material parameters corresponding to relevant sets of experimental data for silicone rubber. By the application of these results, we have demonstrated the variation of the wave characteristics with the level of deformation and propagation direction. Furthermore, we have shown how the extent of entanglements (or entanglement strength  $G_e/G_c$ ) influences the wave propagation in soft elastomers.

Next, we study the shear wave propagation in a class of heterogeneous hyperelastic composites. In particular, we analyze the transversely isotropic fiber composites with phases characterized by the stiffening behavior stemming from the non-Gaussian statistics of polymer chains. We have employed a micromechanics-based approach to derive explicit expressions for phase velocities in terms of volume fraction and

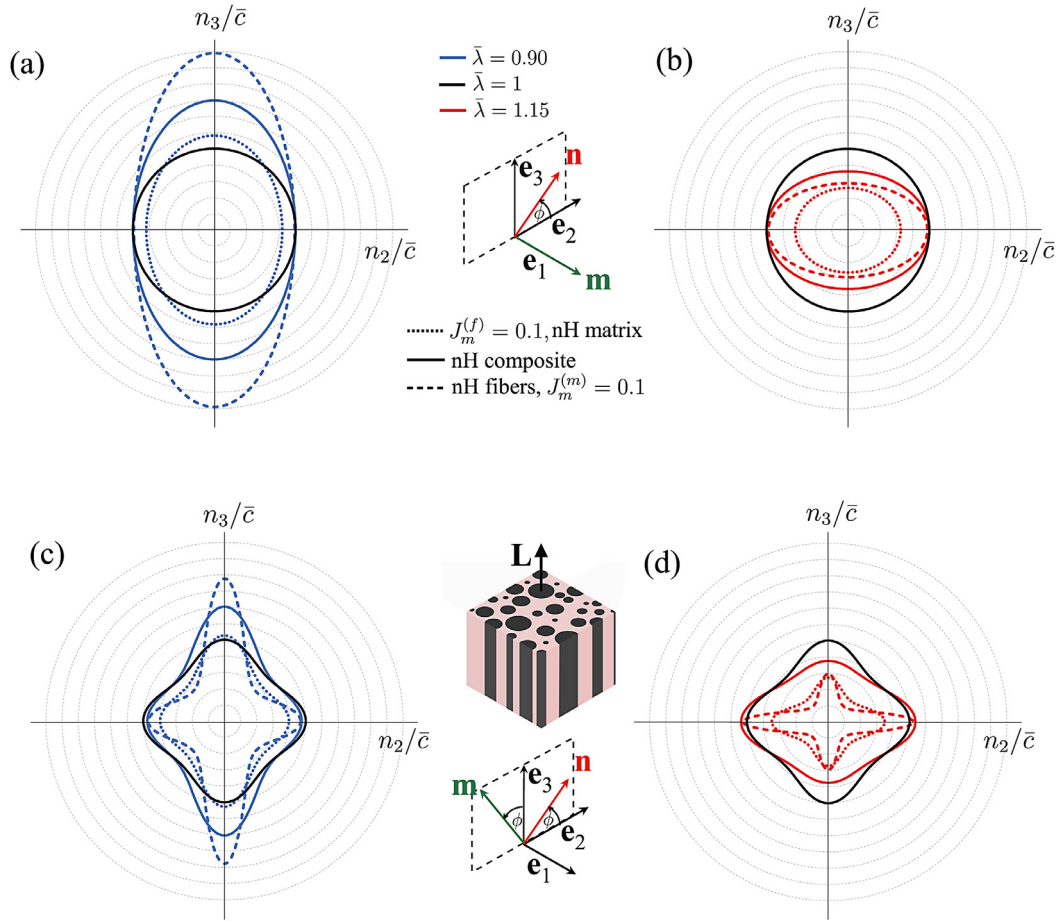


**Fig. 10.** Slowness curves for the out-of-plane (a),(b) and in-plane (c),(d) shear waves. Scale is 0.2 per division. FCs are considered with fiber volume fraction  $v^{(f)} = 0.2$  and initial shear modulus contrast  $\mu^{(f)}/\mu^{(m)} = 10$ . The labels  $n_2/\bar{c}$  and  $n_3/\bar{c}$  are used to represent principal directions of propagation and physical quantity on the polar plot.

material properties of phases. By making use of the derived expressions, we have shown the influence of stiffening behavior varying with the deformation levels and the direction of wave propagation.

We conclude by noting that our results can aid in exploiting the complex multiscale behaviors of soft materials arising from their microstructures, for the design and development of mechano-tunable acoustic materials.

#### Declaration of Competing Interest

The authors declare that they have no known competing financial interests or personal relationships that could have appeared to influence the work reported in this paper.

#### CRediT authorship contribution statement

**Nitesh Arora:** Conceptualization, Methodology, Writing - original draft, Writing - review & editing. **Yuhai Xiang:** Conceptualization, Methodology, Writing - original draft, Writing - review & editing. **Stephan Rudykh:** Conceptualization, Methodology, Writing - original draft, Writing - review & editing, Visualization.

#### Acknowledgments

NA thank the support through LeRoy fellowship.

#### Appendix A. EN material acoustic tensor coefficients in Eq. (17)

Here, we provide the EN material acoustic tensor coefficients  $q_i$ , introduced in of Eq. (17)

$$\begin{aligned} q_1 &= (\mathbf{n} \cdot \mathbf{B} \cdot \mathbf{n})g_1 - (\mathbf{n} \cdot \mathbf{B} \cdot \mathbf{B} \cdot \mathbf{n})g_2, \\ q_2 &= (\mathbf{n} \cdot \mathbf{B} \cdot \mathbf{n})g_2, \\ q_3 &= g_2 + g_3 + 2g_4I_1 + g_5I_1^2, \\ q_4 &= g_4 + g_5I_1, \text{ and} \\ q_5 &= g_5, \end{aligned} \quad (\text{A.1})$$

where,

$$\begin{aligned} g_1 &= 9G_c \frac{1}{(3+I_1/(2N))(3-I_1/N)} \\ &\quad + G_e \frac{(\lambda_1^2\lambda_2^5 + \lambda_2^2\lambda_1^5 + \lambda_1^3\lambda_2^4 + \lambda_2^3\lambda_1^4 + \lambda_1^3\lambda_2 + \lambda_1\lambda_2^3 + \lambda_1^2\lambda_2^2 + \lambda_1 + \lambda_2) + \lambda_1^{-1}\lambda_2^{-1}}{(\lambda_1 + \lambda_2)(\lambda_2\lambda_1^2 + 1)(\lambda_1\lambda_2^2 + 1)}, \\ g_2 &= G_e \frac{\lambda_1\lambda_2(\lambda_1\lambda_2(\lambda_1 + \lambda_2) + 1)}{(\lambda_1 + \lambda_2)(\lambda_2\lambda_1^2 + 1)(\lambda_1\lambda_2^2 + 1)}, \\ g_3 &= 18G_e \frac{(3/(2N) + I_1/N^2)}{(3+I_1/(2N))^2(3-I_1/N)^2} + g_4, \\ g_4 &= -G_e \frac{\lambda_1^4\lambda_2^4(\lambda_1^4\lambda_2^4 + 3\lambda_1^3\lambda_2^3 + 3\lambda_1^2\lambda_2^2 + \lambda_1\lambda_2 + \lambda_2^2 + 3\lambda_1\lambda_2)}{(\lambda_1 + \lambda_2)^3(\lambda_2\lambda_1^2 + 1)^3(\lambda_1\lambda_2^2 + 1)^3}, \\ g_5 &= -G_e \frac{\lambda_1^3\lambda_2^3(\lambda_1\lambda_2(\lambda_1^5\lambda_2^5 + \lambda_1^2\lambda_2^5 + 3\lambda_1^4\lambda_2^4 + 3\lambda_1^3\lambda_2^4 + 3\lambda_1^2\lambda_2^3 + 3\lambda_1\lambda_2^3 + 7\lambda_1^2\lambda_2^2 + 3\lambda_1 + 3\lambda_2) + 1)}{(\lambda_1 + \lambda_2)^3(\lambda_2\lambda_1^2 + 1)^3(\lambda_1\lambda_2^2 + 1)^3} \end{aligned} \quad (\text{A.2})$$

## Appendix B. Phase velocities of *in-plane* shear waves in EN material

Here, we consider the *in-plane* shear waves propagating along  $\mathbf{n} = \cos \theta \mathbf{e}_1 + \sin \theta \mathbf{e}_2$ . The corresponding phase velocities (Eq. (18)) in EN materials undergoing the considered deformation modes are given below.

For uniaxial loading (20)<sub>1</sub>,

$$\begin{aligned} c_u^{(1)} &= \left( \frac{9G_c}{\rho_0} \frac{(\lambda^2 \cos^2 \theta + \lambda^{-1} \sin^2 \theta)}{\Theta_u} + \frac{G_e}{\rho_0} \frac{(\lambda^2 \cos^2 \theta + \lambda^{1/2} \sin^2 \theta + \lambda^2)}{2(\lambda^{3/2} + 1)} \right)^{1/2} \\ c_u^{(2)} &= \left\{ \frac{G_c}{\rho_0} \left[ \frac{9(\lambda^2 \cos^2 \theta + \lambda^{-1} \sin^2 \theta)}{\Theta_u} + \frac{9}{2} \left( \frac{3}{2N} + \frac{\lambda^2 + 2\lambda^{-1}}{N^2} \right) \frac{\lambda^{-2} (\lambda^3 - 1)^2 \sin^2(2\theta)}{\Theta_u^2} \right] \right. \\ &\quad + \frac{G_e}{\rho_0} \left( \frac{1}{2} (\lambda^{1/2} - \lambda^{-1}) \cos(2\theta) \right. \\ &\quad + \frac{1}{32(\lambda^{3/2} + 1)^3} \left[ (3\lambda^2 + 5\lambda + 3\lambda^{1/2} + \lambda^{-1/2} + 4\lambda^{-1})(\lambda^{3/2} - 1)^2 \cos(4\theta) \right. \\ &\quad + 13\lambda^5 - 5\lambda^4 + 31\lambda^2 - 3\lambda + 35\lambda^{7/2} + 9\lambda^{5/2} \\ &\quad \left. \left. \left. + 37\lambda^{1/2} - \lambda^{-1/2} + 12\lambda^{-1} \right) \right] \right) \left. \right\}^{1/2} \end{aligned} \quad (\text{B.1})$$

For equibiaxial loading (20)<sub>2</sub>,

$$\begin{aligned} c_{eb}^{(1)} &= \sqrt{\frac{9G_c}{\rho_0} \frac{\lambda^2}{\Theta_{eb}} + \frac{G_e}{\rho_0} \frac{\lambda^5}{1 + \lambda^3}} \\ c_{eb}^{(2)} &= \sqrt{\frac{9G_c}{\rho_0} \frac{\lambda^2}{\Theta_{eb}} + \frac{G_e}{\rho_0} \frac{1}{2\lambda}} \end{aligned} \quad (\text{B.2})$$

For pure shear deformation (20)<sub>3</sub>,

$$\begin{aligned} c_{ps}^{(1)} &= \left( \frac{9G_c}{\rho_0} \frac{(\lambda^2 \cos^2 \theta + \sin^2 \theta)}{\Theta_{ps}} + \frac{G_e}{\rho_0} \frac{\lambda^2 (\lambda \cos^2 \theta + \sin^2 \theta + \lambda^2)}{(\lambda + 1)(\lambda^2 + 1)} \right)^{1/2} \\ c_{ps}^{(2)} &= \left[ \frac{G_c}{\rho_0} \left( \frac{9(\lambda^2 \cos^2 \theta + \sin^2 \theta)}{\Theta_{ps}} + \frac{9}{2} \left( \frac{3}{2N} + \frac{\lambda^2 + \lambda^{-2} + 1}{N^2} \right) \frac{(\lambda^2 - 1)^2 \sin^2(2\theta)}{\Theta_{ps}^2} \right) \right. \\ &\quad \left. + \frac{G_e}{\rho_0} \frac{((\lambda - 1) \cos(2\theta) + \lambda + 1)^2}{4\lambda(\lambda + 1)} \right]^{1/2} \end{aligned} \quad (\text{B.3})$$

The velocities  $c^{(1)}$  and  $c^{(2)}$  correspond to the wave polarizations  $\mathbf{m} = \mathbf{e}_3$  and  $\mathbf{m} = \sin \theta \mathbf{e}_1 - \cos \theta \mathbf{e}_2$ , respectively. In addition, we use the following quantities in Eqs. (B.1)–(B.3),

$$\begin{aligned} \Theta_u &= (3 + (\lambda^2 + 2\lambda^{-1})/(2N))(3 - (\lambda^2 + 2\lambda^{-1})/N) \\ \Theta_{eb} &= (3 + (2\lambda^2 + \lambda^{-4})/(2N))(3 - (2\lambda^2 + \lambda^{-4})/N) \\ \Theta_{ps} &= (3 + (\lambda^2 + \lambda^{-2} + 1)/(2N))(3 - (\lambda^2 + \lambda^{-2} + 1)/N) \end{aligned} \quad (\text{B.4})$$

## Appendix C. Shear wave velocities in Gent materials

Here, we provide explicit expressions for the phase velocities corresponding to the incompressible Gent materials subjected to three basic deformation modes defined in Eq. (20). In general, the acoustic tensor of Gent model (25) has two distinct nonzero eigenvalues, and hence, there exist two distinct phase velocities (27) corresponding to different polarizations. For some special cases, the value of the velocity is identical. For instance, the shear waves propagating along the principal directions of the left Cauchy-Green deformation tensor ( $\mathbf{n} = \mathbf{e}_i$ ) produce identical phase velocities

$$c_G^{(1)} = c_G^{(2)} = \lambda_i \sqrt{\Theta_G^{-1} \mu J_m / \rho_0}, \quad (\text{C.1})$$

where  $\lambda_i$  ( $i = 1, 2, 3$ ) are the principal stretches in the direction of  $\mathbf{e}_i$ . Consider the shear waves traveling along the direction  $\mathbf{n} = \mathbf{e}_3$ , the phase velocities for three basic deformation states are

$$c_{Gu}^{(1)} = c_{Gu}^{(2)} = \lambda^{-1/2} \sqrt{\Theta_{Gu}^{-1} \mu J_m / \rho_0} \quad (\text{C.2})$$

$$c_{Geb}^{(1)} = c_{Geb}^{(2)} = \lambda^{-2} \sqrt{\Theta_{Geb}^{-1} \mu J_m / \rho_0} \quad (\text{C.3})$$

$$c_{Gps}^{(1)} = c_{Gps}^{(2)} = \lambda^{-1} \sqrt{\Theta_{Gps}^{-1} \mu J_m / \rho_0} \quad (\text{C.4})$$

For the shear waves traveling along  $\mathbf{n} = \cos \theta \mathbf{e}_1 + \sin \theta \mathbf{e}_2$ , the phase velocities also coincide for equi-biaxial deformation ( $\lambda_1 = \lambda_2 = \lambda$ ), namely

$$c_{Geb}^{(1)} = c_{Geb}^{(2)} = \lambda \sqrt{\Theta_{Geb}^{-1} \mu J_m / \rho_0}, \quad (\text{C.5})$$

where  $\Theta_{Geb} = 3 + J_m - (2\lambda^2 + \lambda^{-4})$ .

Next we provide the examples for phase velocities in Gent materials undergoing uniaxial and pure shear deformation modes, for waves propagating in the direction  $\mathbf{n} = \cos \theta \mathbf{e}_1 + \sin \theta \mathbf{e}_2$ . The corresponding phase velocities are

$$\begin{aligned} c_{Gu}^{(1)} &= \sqrt{(\lambda^2 \cos^2 \theta + \lambda^{-1} \sin^2 \theta) \Theta_{Gu}^{-1} \mu J_m / \rho_0} \\ c_{Gu}^{(2)} &= \left( (\lambda^2 \cos^2 \theta + \lambda^{-1} \sin^2 \theta + 0.5 \lambda^{-2} (\lambda^3 - 1)^2 \Theta_{Gu}^{-1} \sin^2(2\theta)) \Theta_{Gu}^{-1} \mu J_m / \rho_0 \right)^{1/2} \end{aligned} \quad (\text{C.6})$$

$$\begin{aligned} c_{Gps}^{(1)} &= \sqrt{(\lambda^2 \cos^2 \theta + \sin^2 \theta) \Theta_{Gps}^{-1} \mu J_m / \rho_0} \\ c_{Gps}^{(2)} &= \left( (\lambda^2 \cos^2 \theta + \sin^2 \theta + 0.5 (\lambda^2 - 1)^2 \Theta_{Gps}^{-1} \sin^2(2\theta)) \Theta_{Gps}^{-1} \mu J_m / \rho_0 \right)^{1/2} \end{aligned} \quad (\text{C.7})$$

where  $\Theta_{Gu} = 3 + J_m - (\lambda^2 + 2\lambda^{-1})$  and  $\Theta_{Gps} = 2 + J_m - (\lambda^2 + \lambda^{-2})$ ; the wave velocities  $c_G^{(1)}$  and  $c_G^{(2)}$  correspond to the waves with polarizations  $\mathbf{m} = \mathbf{e}_3$  and  $\mathbf{m} = \sin \theta \mathbf{e}_1 - \cos \theta \mathbf{e}_2$ , respectively.

## References

- [1] Martin JA, Brandon SC, Keuler EM, Hermus JR, Ehlers AC, Segalman DJ, Allen MS, Thelen DG. Gauging force by tapping tendons. *Nat Commun* 2018;9:1–9.
- [2] Deroy C, Destrade M, Alinden AM, Annaihd AN. Non-invasive evaluation of skin tension lines with elastic waves. *Skin Res Technol* 2017;23:326–35.
- [3] Jiang Y, Li G, Qian L-X, Liang S, Destrade M, Cao Y. Measuring the linear and nonlinear elastic properties of brain tissue with shear waves and inverse analysis. *Biomech model mechanobiol* 2015;14:1119–28.
- [4] Adams SD, Craster RV, Guenneau S. Bloch waves in periodic multi-layered acoustic waveguides. *Proc Royal Soc A Math Phys Eng Sci* 2008;464:2669–92.
- [5] Li G-Y, He Q, Mangan R, Xu G, Mo C, Luo J, Destrade M, Cao Y. Guided waves in pre-stressed hyperelastic plates and tubes: Application to the ultrasound elastography of thin-walled soft materials. *J Mech Phys Solids* 2017;102:67–79.
- [6] Wu B, Su Y, Chen W, Zhang C. On guided circumferential waves in soft electroactive tubes under radially inhomogeneous biasing fields. *J Mech Phys Solids* 2017;99:116–45.
- [7] Sarvazyan AP, Urban MW, Greenleaf JF. Acoustic waves in medical imaging and diagnostics. *Ultrasound Med Biol* 2013;39:1133–46.
- [8] Wang Y-F, Wang Y-Z, Wu B, Chen W, Wang YS. Tunable and active phononic crystals and metamaterials. *Appl Mech Rev* 2020;72.
- [9] Kushwaha M, Halevi P, Dobrzynski L, Djafari-Rouhani B. Acoustic band structure of periodic elastic composites. *Phys Rev Lett* 1993;71:2022–5.
- [10] Zhang S, Xia C, Fang N. Broadband acoustic cloak for ultrasound waves. *Phys Rev Lett* 2011;106:024301.
- [11] Lee SH, Park CM, Seo YM, Wang ZG, Kim CK. Composite acoustic medium with simultaneously negative density and modulus. *Phys Rev Lett* 2010;104:054301.
- [12] Fang N, Xi D, Xu J, Ambati M, Srituravanich W, Sun C, Zhang X. Ultrasonic metamaterials with negative modulus. *Nat Mater* 2006;5:452–6.
- [13] Zhou W, Wu B, Muhammad, Du Q, Huang G, Lü C, Chen W. Actively tunable transverse waves in soft membrane-type acoustic metamaterials. *J Appl Phys* 2018;123:165304.
- [14] Bertoldi K, Boyce MC. Wave propagation and instabilities in monolithic and periodically structured elastomeric materials undergoing large deformations. *Phys Rev B* 2008;78:184107.
- [15] Slesarenko V, Galich PI, Li J, Fang NX, Rudykh S. Foreshadowing elastic instabilities by negative group velocity in soft composites. *Appl Phys Lett* 2018;113:031901.
- [16] Li J, Slesarenko V, Rudykh S. Auxetic multiphase soft composite material design through instabilities with application for acoustic metamaterials. *Soft Matter* 2018;14:6171–80.
- [17] Rudykh S, Boyce M. Transforming wave propagation in layered media via instability-induced interfacial wrinkling. *Phys Rev Lett* 2014;112:034301.



- [18] Dorfmann A, Ogden RW. Electroelastic waves in a finitely deformed electroactive material. *IMA J Appl Math* 2010;75:604–36.
- [19] Galich PI, Rudykh S. Manipulating pressure and shear elastic waves in dielectric elastomers via external electric stimuli. *Int J Solids Struct* 2016;91:18–25.
- [20] Chang Z, Guo H-Y, Li B, Feng XQ. Disentangling longitudinal and shear elastic waves by neo-hookean soft devices. *Appl Phys Lett* 2015;106:161903.
- [21] Galich PI, Rudykh S. Comment on "Disentangling longitudinal and shear elastic waves by neo-Hookean soft devices" [Appl. Phys. Lett. 106, 161903 (2015)]. *Appl Phys Lett* 2015;107:056101.
- [22] Pelrine RE, Kornbluh RD, Joseph JP. Electrostriction of polymer dielectrics with compliant electrodes as a mean of actuation. *Sens Actuator A* 1998;64:77–85.
- [23] Huang J, Lu T, Zhu J, Clarke DR, Suo Z. Large, uni-directional actuation in dielectric elastomers achieved by fiber stiffening. *Appl Phys Lett* 2012;100.
- [24] Ginder J, Clark S, Schlotter W, Nichols M. Magnetostrictive phenomena in magnetorheological elastomers. *Int J Modern Phys B* 2002;16:2412–18.
- [25] Yu Y, Nakano M, Ikeda T. Directed bending of a polymer film by light. *Nature* 2003;425. 145–145
- [26] Acome E, Mitchell S, Morrissey T, Emmett M, Benjamin C, King M, Radakovitz M, Keplinger C. Hydraulically amplified self-healing electrostatic actuators with muscle-like performance. *Science* 2018;359:61–5.
- [27] Rothemund P, Kellaris N, Mitchell SK, Acome E, Keplinger C. Hasel artificial muscles for a new generation of lifelike robots recent progress and future opportunities. *Adv Mater* 2020;2003375.
- [28] Arora N, Kumar P, Joglekar MM. A modulated voltage waveform for enhancing the travel range of dielectric elastomer actuators. *J Appl Mech* 2018;85.
- [29] Mohammadi NK, Galich PI, Krushynska AO, Rudykh S. Soft magnetoactive laminates: large deformations, transverse elastic waves and band gaps tunability by a magnetic field. *J Appl Mech* 2019;86.
- [30] Saxena P, Ogden RW. On love-type waves in a finitely deformed magnetoelastic layered half-space. *Zeitschrift für angewandte Mathematik und Physik* 2012;63:1177–200.
- [31] Yu K, Fang NX, Huang G, Wang Q. Magnetoactive acoustic metamaterials. *Adv Mater* 2018;30:1706348.
- [32] Destrade M, Ogden RW. On magneto-acoustic waves in finitely deformed elastic solids. *Math Mech Solids* 2011;16:594–604.
- [33] Humphrey JD. *Cardiovascular Solid Mechanics: cells, tissues, and organs*. New York: Springer-Verlag; 2002.
- [34] Goulet F, Rancourt D, Cloutier R, Germain L, Poole AR, Auger FA. Tendons and ligaments. *Principles of tissue engineering* 2000:633–43.
- [35] Langley NR, Polmanteer KE. Relation of elastic modulus to crosslink and entanglement concentrations in rubber networks. *Journal of Polymer Science: Polymer Physics Edition* 1974;12:1023–34.
- [36] Gula IA, Karimi-Varzaneh HA, Svaneborg C. Computational study of the cross-link and the entanglement contributions to the elastic properties of model pdms networks. *arXiv preprint arXiv:200406473* 2020.
- [37] Garcia R, Pizzi A. Crosslinked and entanglement networks in thermomechanical analysis of polycondensation resins. *J Appl poly sci* 1998;70:1111–19.
- [38] Edwards S. The statistical mechanics of polymerized material. *Proc Phys Soc* 1967;92:9.
- [39] Marrucci G. Rubber elasticity theory. a network of entangled chains. *Macromolecules* 1981;14:434–42.
- [40] Mullins L. Softening of rubber by deformation. *Rubber chemistry and technology* 1969;42:339–62.
- [41] Horgan CO, Saccomandi G. Phenomenological hyperelastic strain-stiffening constitutive models for rubber. *Rubber Chem Technol* 2006;79:152–69.
- [42] Mason P. Thermal expansion and viscoelasticity of rubber in relation to crosslinking and molecular packing. *Polymer* 1964;5:625–35.
- [43] Holzapfel GA, et al. *Biomechanics of soft tissue. The handbook of materials behavior models* 2001;3:1049–63.
- [44] Biot MA. Non linear theory of elasticity and the linearized case for a body under initial stress. *Philos Mag* 1939;XXVII:468–89.
- [45] Destrade M, Ogden RW. On stress-dependent elastic moduli and wave speeds. *J Appl Math* 2013;78:965–97.
- [46] Scott N, Hayes M. Small vibrations of a fibre-reinforced composite. *Q J Mech Appl Math* 1976;29:467–86.
- [47] Truesdell C, Noll W. *The non-linear field theories of mechanics*. Springer; 1965.
- [48] Scott N. Small vibrations of prestrained constrained elastic materials: The idealized fibre-reinforced material. *Int J Solids Struct* 1991;27:1969–80.
- [49] Scott N. Waves in a homogeneously prestrained incompressible, almost inextensible, fibre-reinforced elastic material. *Proc R Irish Acad Sect A* 1992;92A:9–36.
- [50] Ogden R, Singh B. Propagation of waves in an incompressible transversely isotropic elastic solid with initial stress: Biot revisited. *J Mech Mater Struct* 2011;6:453–77.
- [51] Vinh PC, Merodio J. On acoustoelasticity and the elastic constants of soft biological tissues. *J Mech Mater Struct* 2013;8:359–67.
- [52] Nam NT, Merodio J, Vinh PC. The secular equation for non-principal rayleigh waves in deformed incompressible doubly fiber-reinforced nonlinearly elastic solids. *Int J Non-Linear Mech* 2016;84:23–30.
- [53] Vinh PC, Merodio J, Hue TTT, Nam NT. Non-principal rayleigh waves in deformed transversely isotropic incompressible non-linearly elastic solids. *IMA J Appl Math* 2014;79:915–28.
- [54] Galich PI, Slesarenko V, Rudykh S. Shear wave propagation in finitely deformed 3D fiber-reinforced composites. *Int J Solids Struct* 2017;110-111:294–304.
- [55] Galich PI, Slesarenko V, Li J, Rudykh S. Elastic instabilities and shear waves in hyperelastic composites with various periodic fiber arrangements. *Int J Eng Sci* 2018;130:51–61.
- [56] Treloar LRG. *The Physics of Rubber Elasticity*. Clarendon Press, Oxford; 1975.
- [57] Xiang Y, Zhong D, Wang P, Mao G, Yu H, Qu S. A general constitutive model of soft elastomers. *J Mech Phys Solids* 2018;117:110–22.
- [58] Gent A. A new constitutive relation for rubber. *Rubber Chem Technol* 1996;69:59–61.
- [59] Galich PI, Rudykh S. Influence of stiffening on elastic wave propagation in extremely deformed soft matter: from nearly incompressible to auxetic materials. *Extreme Mech Lett* 2015;4:156–61.
- [60] Arora N, Li J, Slesarenko V, Rudykh S. Microscopic and long-wave instabilities in 3d fiber composites with non-gaussian hyperelastic phases. *Int J Eng Sci* 2020;157:103408.
- [61] Drygaś P, Gluzman S, Mityushev V, Nawalaniec W. *Applied Analysis of Composite Media: Analytical and Computational Results for Materials Scientists and Engineers*. Woodhead Publishing; 2019.
- [62] Rudykh S, deBotton G. Instabilities of hyperelastic fiber composites: micromechanical versus numerical analyses. *J Elasticity* 2012;106:123–47.